MODELING OF HIGH ENTHALPY FLOWS FOR HYPERSONIC RE-ENTRY AND GROUND-BASED ARC-JET TESTING

BY

AMAL SAHAI

THESIS

Submitted in partial fulfillment of the requirements
for the degree of Master of Science in Aerospace Engineering
in the Graduate College of the
University of Illinois at Urbana-Champaign, 2015

Urbana, Illinois

Master's Committee:

Professor Marco Panesi

Abstract

This work presents a simulation framework for modeling high enthalpy ionized gas flows during planetary entry flights and ground-based arc-jet testing. The system of Favre-averaged Navier-Stokes equations in thermo-chemical non-equilibrium with Spalart-Allmaras turbulence closure is outlined, along with models for thermodynamics, chemical kinetics, transport properties, and the applied electric field. The electric field and the Joule heating term are computed using a Poisson equation and the generalized Ohm's law. A standard two-temperature model is implemented to account for non-equilibrium effects. A numerical method based on the streamline upwind Petrov-Galerkin (SUPG) finite element formulation is utilized. A two-way loose coupling strategy between the flow solver and the electric field is introduced to achieve convergence. The methodology is first tested by modeling hypersonic axisymmetric flows over a blunt body for a range of increasingly complex flight conditions. We then apply it to simulate the flow-field and electrical discharge inside the 20 MW NASA Ames Aerodynamic Heating facility (AHF) to further confirm the capabilities and robustness of the developed framework.

"It was the best of times, it was the worst of times"

— Charles Dickens, *A Tale of Two Cities*

Acknowledgments

I have had the distinct privilege of working with numerous distinguished researchers during the course of the present study. Any semblance of progress that I have made over the last two years is a direct consequence of the assistance I have received from these brilliant individuals. I would first like to thank my master's advisor, Dr. Marco Panesi, for his continuous encouragement and guidance during the period of my study. I would also like to express my gratitude towards Dr. Benjamin Kirk, NASA Johnson Space Center, and Dr. Nagi Mansour, NASA Ames Research Center, for their constant support, which has been critical for completing the current work. I am greatly indebted to Dr. Roy Stogner, University of Texas at Austin, Dr. Alessandro Munafo, and Mahesh Natarajan for patiently answering my queries. I would like to thank my current and former lab mates Kevin Heritier, Robyn MacDonald, Wenbo Zhang, Andrea Alberti, and Vegnesh Jayaraman for all their help. Finally, I would like to acknowledge with gratitude, the support and love of my family – my parents and sister, which has sustained me throughout my life.

Table of Contents

List of Figures

Chapter 1

Introduction

1.1 Introduction

The entry of space vehicles into a planetary atmosphere from outer space occurs at hypersonic speeds. The vehicle encounters denser atmospheric layers as it progresses towards the surface, dissipating its kinetic energy through drag. A strong bow shock develops in front of the capsule which heats up the gas to several thousand degrees Kelvin. The sudden temperature jump, experienced by the flow, brings about strong collisions among the gas particles, provoking changes in chemical composition of the gas and exciting the internal energy modes of its atoms and molecules. At sufficiently high temperatures, the gas ionizes and the flow becomes a weakly ionized plasma. The radiation emitted and absorbed by the gas can also play an important role in the distribution of energy around the vehicle at such high temperatures. The different physical and chemical phenomena occurring during atmospheric entry are outlined in Figure 1.1. Thermal and chemical processes require a finite amount of time to occur. When the characteristic time of these processes is of the same order as the flow characteristic time, a state of thermal (internal modes out of equilibrium with the translational mode) and chemical non-equilibrium is reached by the gas. The characterization of the non-equilibrium phenomena occurring in the flow strongly affects the total convective and radiative heating experienced by the vehicle during the entry phase.

The spacecraft is protected from this harsh environment by using thermal protection systems (TPS), which are critical for reducing and dissipating the large heat fluxes being received by the entry capsule. The heat loads experienced during entry dictate the choice of the TPS and ultimately drive the overall design process for the protection of the vehicle. Thus, in order to design reliable

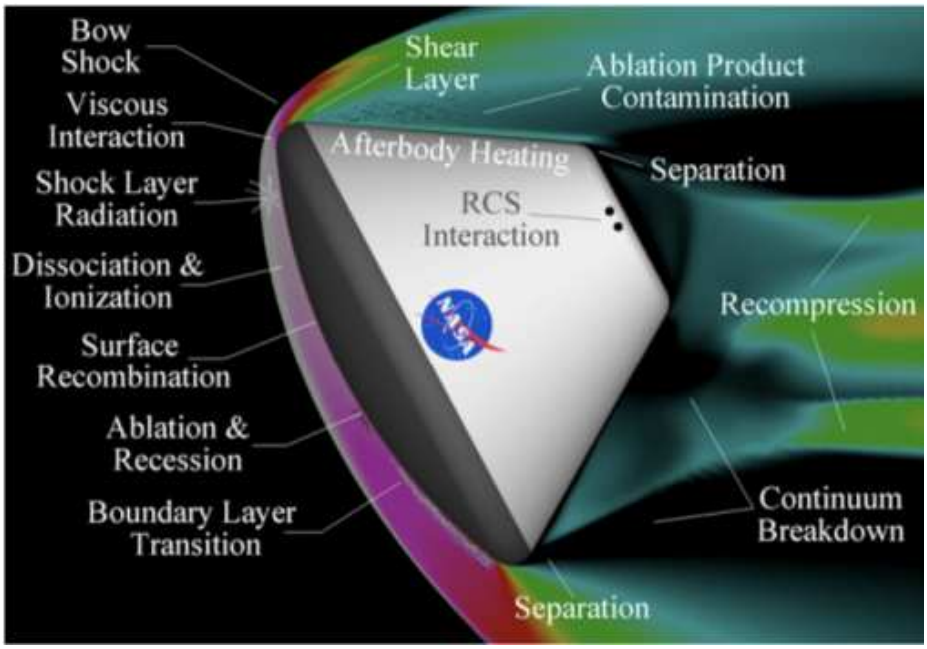

Figure 1.1: Flowfield during hypersonic vehicular planetary entry.
(Source: NASA)

spacecraft, the heat flux distribution over the heat-shield must be accurately characterized. Traditionally, this has been achieved through extensive wind tunnel testing. Conventional wind tunnel facilities are not capable of replicating conditions during non-equilibrium high speed entries for a significant duration in time. Arc-jets and inductively coupled plasma (ICP) heaters are capable of generating high enthalpy flows which provide the necessary temperature levels and heating rates. In these high enthalpy facilities, an electro-magnetic discharge heats up the gas, generating a plasma flow. This hot gas mixture is typically accelerated by means of a converging- diverging nozzle into the test chamber where the actual testing takes place.

Since, the exact flight conditions cannot be replicated for the entire vehicle, the objective is to match physical parameters for critical parts of the heat-shield. An example of this is stagnation line testing, which aims at reproducing heating rates at the stagnation point region [1]. The link between in-flight and experimental conditions is established on the basis of approximate theories,

like Local Heat Transfer Simulation (LHTS) [2], to reconstruct flight conditions using overly simplified assumptions. A better approach is to apply the same computational and physical models to both flight and ground-based testing. The advent of powerful computing capabilities enables Computational Fluid Dynamics (CFD) simulations that can capture the complex physics of both entry flight and ground-based test facilities. The present work aims at creating an integrated simulation framework for high fidelity CFD analysis of both hypersonic entry and ground-based testing, with accurate physical models for the description of the thermodynamic, chemical, non-equilibrium (NLTE) energy transfer and transport properties of high temperature gaseous mixtures, and the associated electric field (for arc-jet flows).

Continuous finite element methods as a discretization tool have largely been overlooked in favor of finite volume methods in numerical solvers investigating different classes of flows. This trend is now changing with advancements being made in the development of stabilized finite element techniques, especially for hypersonic applications. The fully-Implicit Navier-Stokes (FINS-S) [3, 4] hypersonic solver, a parallel, adaptive, unstructured, finite element based solver built using the LIBMESH framework [5], represents the state of the art of hypersonic solvers due to its advanced numerical capabilities. Recently, FIN-S has been coupled with CANTERA for simulating chemically reacting flows [6]. CANTERA is a widely used software library, for the calculation of thermodynamics, chemistry and transport phenomenon [7]. Unfortunately, CANTERA, in its present form, cannot simulate weakly ionized plasmas. Thus, FIN-S, despite its sophisticated numerical algorithms, is limited to modeling low speed entry problems (e.g. Low Earth Orbit (LEO) entry conditions) [8]. The present work addresses this shortcoming by implementing improved physical models for weakly ionized plasmas for flight conditions relevant to Mars and lunar return entry applications [9, 10, 11]. The new library, that supplies FIN-S with the necessary information pertaining to the gaseous mixture, is hosted in MUTATION++ [12], a C++ library being developed at the von Karman Institute, Belgium, to model Local Thermodynamic Equilibrium chemically reacting flows.

In this work, we will simulate and present results from the new capability for the FIRE II lunar return conditions, and the flow in arc-heaters, with regards to modeling high enthalpy flows in

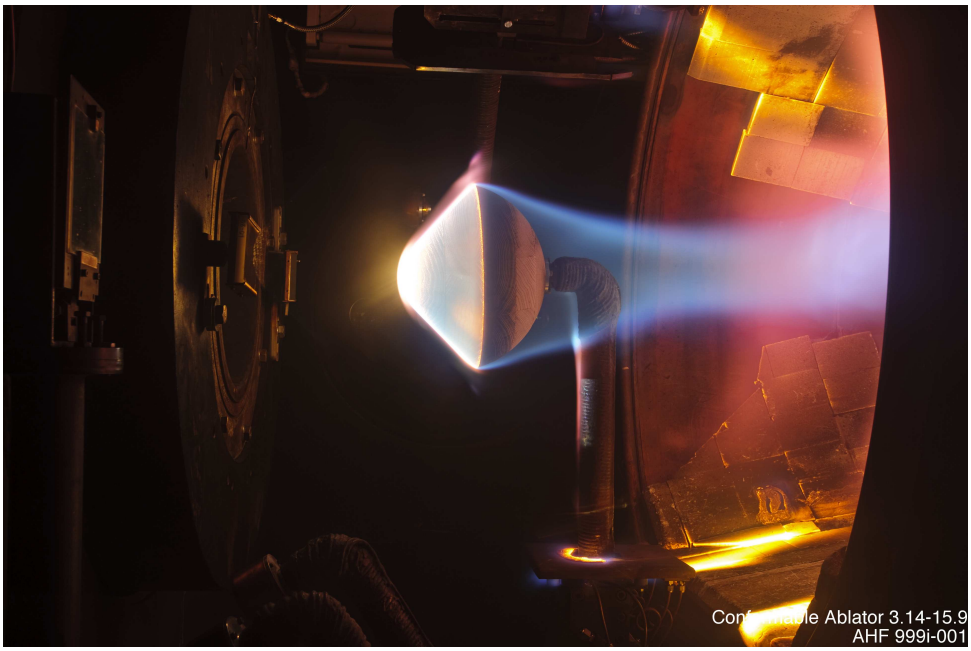

Figure 1.2: SPRITE model under test in the NASA Ames 20 MW Aerodynamic Heating Facility. (Source: NASA Ames Research Center)

ground-based test facilities. The second numerical investigation focuses on the 20 MW Aerodynamic Heating Facility (AHF) at NASA Ames Research Center (Figure 1.2). The AHF is a segmented-type arc heater which comprises of a constricted-arc heater section (anode, cathode, and constrictor), a nozzle section, and a test chamber [13]. The electric discharge causes the incoming gas to heat up. The high pressure in the heater section ensures that the flow is in local thermal equilibrium (LTE). However, the acceleration in the converging-diverging nozzle causes the density to decrease along with the collision frequency, leading to thermochemical non-equilibrium. The flow chemistry freezes while traveling through the nozzle. The flow then enters a large chamber where sample testing is carried out.

Test planning and the design of arc-jet facilities require accurate characterization of the physical properties of the flow at the nozzle exit, deeming the complete modeling of the different phenomenon, that manifest in the flow-field, critical to the overall success of this endeavor. Despite the spurt in

research targeting this problem, there are only a few CFD codes that attempt to solve for these physical processes through an integrated analysis. The current investigation attempts to create a *two-way* coupling between the electric field and the corresponding arc discharge, and the flow-field. The intense electric currents result in energy being added through Joule heating which subsequently affects the value of electrical conductivity and causes the electric field to continue evolving along with the flow. A separate module for computing the electric field and the resultant Joule heating term is added to FIN-S. Additionally, the Spalart-Allmaras turbulence model is used to account for the effect of turbulence. FIN-S is therefore, used to model the entire range of flows – subsonic in the electric heater, supersonic at the nozzle exit, and hypersonic flows for free flight simulations. The application of the same physical models and numerical techniques will aid in establishing a link between subsonic and hypersonic flows. This can be utilized for developing operating characteristics for ground-based test facilities for given flight conditions and for interpreting experimental data from test facilities.

1.2 Thesis Outline

This thesis presents an overview of the governing equations, the numerical solution procedure, and two investigations related to flight conditions and ground-based facilities. Chapter 2 describes the set of governing equations and property models used to describe flows in chemical and thermal non-equilibrium. This chapter also presents a simplified formulation for the electric field equation and the Joule heating term, along with the turbulence model used in this study. The stabilized finite element technique in FIN-S is detailed in Chapter 3. The time-integration strategy and treatment of the boundary conditions are also discussed in Chapter 3. The results obtained for free flight and ground-based arc-jet testing are summarized in Chapter 4. Finally, conclusions and a description of future work is presented in Chapter 5.

Chapter 2

Physical Model

The flow governing equations comprise of species mass conservation, momentum conservation and energy conservation equations. These conservation equations can be obtained by taking successive moments of the Boltzmann equation. The description for the flow field generated in an arc-heated wind tunnel requires an additional coupling with the Maxwell equations governing the electromagnetic fields that sustain the plasma discharge. Under an imposed electric field assumption, the two sets of equations are coupled through electrical conductivity, that is present in the electric field equation and the Joule heating term (on the flow side).

To solve the governing equations expressions for thermodynamic and transport properties are required. In this work, a two-temperature model is used to model thermal nonequilibrium effects. It is assumed that:

- the rotational states are in equilibrium with the heavy particle translational energies characterized by a common translational-rotational temperature, T_{hr} / T ;
- and the electronic energies of the heavy particles and vibrational energies of the molecular mixture components are equilibrated with the translational energies and are defined by a common electronic-vibrational temperature, T_{ev} / T_v .

The full Maxwell equations, in the absence of a strong plasma induced magnetic field, can be simplified further to obtain a Poisson equation. Thus, the final form of the governing equations closely resemble the Navier-Stokes equations, supplemented by the generalized Ohm's law and the electric field equation.

2.1 Governing Magneto-Hydrodynamics Equations

2.1.1 Hydrodynamics Conservation Equations

A simplified representation that disregards the internal degrees of freedom is used for describing the ionized plasma mixture. The distribution of s-particles in the phase space, $(d\overrightarrow{r_s}, d\overrightarrow{w_s})$ is represented with the distribution function, $f_s(\overrightarrow{r_s}, \overrightarrow{w_s})$, and satisfies the Boltzmann's equation:

$$\frac{\partial f_s}{\partial t} + \overrightarrow{w_s} \cdot \nabla f_s + \frac{1}{m_s} \overrightarrow{F_s} \cdot \nabla_{\overrightarrow{w_s}} f_s = \left[\frac{\partial f_s}{\partial t}\right]_{el} + \left[\frac{\partial f_s}{\partial t}\right]_{ch} \tag{2.1}$$

where $\overrightarrow{F_s}$ is the Lorentz-force on the s-particles, with the effect of other body forces like gravity neglected. The terms on the right hand side represent the net production of particles due to elastic and inelastic collisions respectively.

The hydrodynamic equations required for the mathematical modeling of high-enthalpy flows are derived by taking the moments of mass, momentum, and energy of the Boltzmann equation (Equation 2.1). Equation 2.1 is multiplied by θ_s and integrated over $\overrightarrow{w_s}$ to obtain Enskog's equation:

$$\frac{\partial}{\partial t}(n_s \langle\theta\rangle_s) + \nabla \cdot (n_s \langle\overrightarrow{w}\theta\rangle_s) - \frac{n_s}{m_s}\left\langle \overrightarrow{F_s} \cdot \nabla_{\overrightarrow{w_s}}\theta \right\rangle_s = \int \theta_s \left[\frac{\partial f_s}{\partial t}\right]_{el} d\overrightarrow{w_s} + \int \theta_s \left[\frac{\partial f_s}{\partial t}\right]_{ch} d\overrightarrow{w_s} \tag{2.2}$$

where a molecular quantity enclosed within the parenthesis $\langle\cdot\rangle$ represents its averaged value.

Continuity Equation

Mass continuity equations for individual mixture constituents are critical for computing the mixture composition. The n species continuity equations are obtained by assuming $\theta = m_s$:

$$\frac{\partial \rho_s}{\partial t} + \nabla \cdot \left[\rho_s \left(\overrightarrow{u} + \overrightarrow{U_s}\right)\right] = \omega_s \tag{2.3}$$

where ω_s represents species' net production rate through chemical reactions and $\overrightarrow{U_s}$ is the diffusive velocity of species s. The mixture continuity equation is obtained by adding up Equation 2.3 over

all species:

$$\frac{\partial \rho}{\partial t} + \nabla \cdot (\rho \overrightarrow{u}) = 0 \tag{2.4}$$

The chemical source term on the right hand side disappears because total mass is conserved for the complete system.

Momentum Equation

The species momentum equation is obtained when $\theta_s = m_s \overrightarrow{w_s}$. By adding up the momentum equations for the n individual mixture components, the mixture momentum equation is obtained:

$$\frac{\partial \rho \overrightarrow{u}}{\partial t} + \nabla \cdot \left(\rho \overrightarrow{u} \overrightarrow{u} + p\hat{I} - \hat{\tau} \right) = \overrightarrow{E}' n_c + \overrightarrow{J} \times \overrightarrow{B} \tag{2.5}$$

where $\hat{\tau}$ is the viscous stress tensor. The effect of the Lorentz force, $\overrightarrow{E}' n_c + \overrightarrow{J} \times \overrightarrow{B}$, is neglected since the mixture is considered to be quasi-neutral and the imposed arc current is the dominant electric current.

Total Energy Equation

$\theta_s = m_s w_s^2/2$ gives the total energy equation for individual species. These can be summed to obtain the equation for the mixture:

$$\frac{\partial \rho e}{\partial t} + \nabla \cdot (\rho \overrightarrow{u} h) + \nabla \cdot \left(\sum_s \rho_s \overrightarrow{U_s} h_s \right) + \nabla \cdot \overrightarrow{q} = \nabla \cdot (\overrightarrow{u} : \hat{\tau}) + \overrightarrow{J} \cdot \overrightarrow{E} \tag{2.6}$$

where the total energy per unit mass is defined as $E = u^2/2 + e$ and the total enthalpy per unit mass is written as $H = u^2/2 + h$. $\overrightarrow{J} \cdot \overrightarrow{E}$ is the contribution of the Joule heating.

2.1.2 Electric Field and Current

We assume that the imposed electric field is the dominant field and that the electric current generated by flow of the plasma is too small to induce a strong enough magnetic field. Thus, a simplified

electric field equation, that is derived from the full Maxwell equations and generalized Ohm's law, can be used to model the arc dynamics.

Ohm's Law

The electric field $\overrightarrow{E}$ can be expressed as the sum of an irrotational electrostatic part $\overrightarrow{E_S}$ and a divergence-free induced part $\overrightarrow{E_I}$:

$$\overrightarrow{E} = \overrightarrow{E_S} + \overrightarrow{E_I} \tag{2.7}$$

where $\overrightarrow{E_S} = -\nabla\phi$ and $\overrightarrow{E_I} = -\frac{\partial \overrightarrow{A}}{\partial t}$. $\overrightarrow{E_I} = 0$, due to the absence of an effective induced magnetic field in the arc-heated wind tunnel facility. The conduction current in unmagnetized plasmas is mostly due to the flow of light electrons (and not heavy ions) and can be expressed as:

$$\overrightarrow{J} = \sum_s n_s \overrightarrow{U_s} q_s \approx n_e \overrightarrow{U_e} q_e = \overrightarrow{J_e}. \tag{2.8}$$

$\overrightarrow{J}$ can then be expressed using Ohm's law:

$$\begin{aligned} \overrightarrow{J} &= \sigma\left(\overrightarrow{E_S} + \cancel{\overrightarrow{E_I}} + \cancel{\overrightarrow{u} \times \overrightarrow{B}}\right) \\ &= \sigma\left(-\nabla\phi\right) \end{aligned} \tag{2.9}$$

where $\sigma = \frac{n_e^2 q_e^2}{p_e \sum_{j \neq e} x_j D_{ej}}$, is the electrical conductivity.

Electric Field Equation

The electric field equation is obtained by taking the divergence of the Ampere's circuital law equation while neglecting the displacement current:

$$\nabla . \left[\sigma\left(\nabla\phi\right)\right] = 0 \tag{2.10}$$

The electric field $\overrightarrow{E}$ and Joule heating rate $\dot{\mathcal{S}}_{joule}$ are computed as:

$$\overrightarrow{E} = -\nabla\phi \tag{2.11}$$

$$\overrightarrow{J} = \sigma\,\overrightarrow{E} \tag{2.12}$$

$$\begin{aligned}\dot{\mathcal{S}}_{joule} &= \overrightarrow{J}\,.\,\overrightarrow{E} \\ &= \sigma\,(\nabla\phi\,.\,\nabla\phi)\end{aligned} \tag{2.13}$$

2.2 Thermodynamic Properties

A detailed description of the different thermodynamic models that have been used for predicting the properties of air plasmas can be found in [14, 15, 16]. Molecules and atoms have discrete internal energy modes, which can be computed using quantum physics. The thermodynamic properties of plasmas in the current work are evaluated using a more realistic description that includes these energy modes. Diatomic molecules are modeled using the rigid rotor harmonic oscillator model. This allows the different energy modes, namely rotational, vibrational, and electronic, to become decoupled from one another. It has been shown that the error in the calculated mixture properties originating from neglecting this coupling, for the class of flows being investigated, is of the order of 1%. Thus, thermodynamic properties of individual species (and the mixture) can be evaluated using straightforward statistical mechanics formulations [17]. A further simplification is obtained by taking into account only a finite number of electronic levels [16]. Therefore, only a minimum number of electronic levels that produce a non-negligible change of energy in the temperature range encountered during the course of this study, are considered while computing electronic energy. The hydrodynamics equations derived in the preceding section can be extended to a more accurate form by including the effect of internal degrees of freedom.

Three different mixture models are used in the present work:

1. **Air-11**:
    - Neutral species: N_2, O_2, NO, N, O

- Charged species: N_2^+, O_2^+, NO^+, N^+, O^+, e^-.

2. **Air-5**: N_2, O_2, NO, N, O (only neutral species).

3. **Argon-3**: Ar, Ar^+, e^-.

The computationally cheaper three-species argon model has been employed to expedite the process of developing the multi-physics framework for simulating plasma-heated wind tunnel flows.

2.2.1 Statistical Mechanics

The population of the excited states is estimated using a two-temperature Boltzmann distribution:

$$\frac{n_s^{r,v,e}}{n_s} = \frac{g_{rot,s}^r g_{vib,s}^v g_{el,s}^e exp\left(-\epsilon_{rot,s}^r / k_B T_{hr}\right) exp\left(-\left(\epsilon_{vib,s}^v + \epsilon_{el,s}^e\right) / k_B T_{ev}\right)}{Q_{rot,s} Q_{vib,s} Q_{el,s}} \tag{2.14}$$

where $n_s^{r,v,e}$ denotes the number density of the s particles in the (r, v, e) quantum state. $Q_{rot,s}$, $Q_{vib,s}$ and $Q_{el,s}$ represent the partition functions and are defined as:

$$Q_{M,s} = \sum_{m=0}^{\infty} g_{M,s}^m exp\left(-\epsilon_{M,s}^m / k_B T_M\right) \tag{2.15}$$

Rotational Energy

$Q_{rot,s}$ can be evaluated as:

$$Q_{rot,s} = \frac{T_{hr}}{\sigma_s \theta_{rot,s}} + \frac{1}{3\sigma_s} + \frac{\theta_{rot,s}}{15\sigma_s T_{hr}} \tag{2.16}$$

where $\theta_{rot,s}$ represents the characteristic temperature of rotational energy and σ_s is the symmetry number. The rotational energy per unit mass of molecular species s can be expressed as:

$$e_{rot,s} = \left(k_B / m_s\right) T_{hr} \left(1 - \frac{\theta_{rot,s}}{\theta_{rot,s} + 3T_{rot,s}}\right). \tag{2.17}$$

Vibrational Energy

The expression for $Q_{vib,s}$ is given by:

$$Q_{vib,s} = \frac{1}{1 - exp\left(-\sigma_{vib,s}/T_{ev}\right)} \tag{2.18}$$

where $\theta_{vib,s}$ defines the characteristic vibrational temperature. The vibrational energy per unit mass of molecular species s can then be defined as:

$$e_{vib,s} = \left(k_B/m_s\right) \frac{\theta_{vib,s}}{exp\left(\theta_{vib,s}/T_{ev} - 1\right)}. \tag{2.19}$$

Electronic Energy

There is no complete analytical expression for computing the total energy associated with all electronic states for a given chemical species. The electronic energy is evaluated using an explicit formula:

$$Q_{el,s} = \sum_{e=0}^{\infty} g^e_{el,s} exp\left(-\epsilon^e_{el,s}/k_B T_{ev}\right). \tag{2.20}$$

As discussed before, this summation can be truncated at a maximum energy level $e_{max,s}$ with minimal impact on accuracy. The electronic energy per unit mass is defined as:

$$e_{el,s} = \left(k_B/m_s\right) \frac{\sum_{e=0}^{e_{max,s}} g^e_{el,s} \epsilon^e_{el,s} exp\left(-\sigma^e_{el,s}/k_B T_{ev}\right)}{k_B Q_{el,s}}. \tag{2.21}$$

2.2.2 Hydrodynamics Equations with the two-temperature model

The previously derived hydrodynamics governing equations for the flow-field can be expanded to include the internal degrees of freedom. The inelastic collisions between quantum states are treated as chemical reactions. Elastic collisions between species are considered to be independent of their quantum states (Eucken assumption). The process of energy exchange between different internal modes is described using simplified models for the different types of interactions.

Continuity

The continuity equation for particles of species s in a particular quantum state is:

$$\frac{\partial \rho_s^{r,v,e}}{\partial t} + \nabla \cdot \left[\rho_s^{r,v,e} \left(\overrightarrow{u} + \overrightarrow{U_s^{r,v,e}} \right) \right] = \omega_s^{r,v,e}. \tag{2.22}$$

The continuity equations for species s can then be obtained by adding up the above equation for all quantum states:

$$\frac{\partial \rho_s}{\partial t} + \nabla \cdot \left[\rho_s \left(\overrightarrow{u} + \overrightarrow{U_s} \right) \right] = \omega_s \tag{2.23}$$

$$\overrightarrow{U_s} = (1/\rho_s) \sum_{r,v,e} \rho_s^{r,v,e} \overrightarrow{U_s^{r,v,e}}. \tag{2.24}$$

Momentum

The mixture momentum equation derived for the plasma heated flows requires no modification:

$$\frac{\partial \rho \overrightarrow{u}}{\partial t} + \nabla \cdot \left(\rho \overrightarrow{u} \overrightarrow{u} + p\hat{I} - \hat{\tau} \right) = 0 \tag{2.25}$$

Internal Mode Energy

The total internal energy associated with any given mode M (rotational, vibrational, electronic) for an individual species can be obtained by summing over all quantum states for that mode. The mixture internal energy for a mode is given by $e_M = \sum_s y_s e_{M,s}$ and the corresponding governing equation is:

$$\frac{\partial \rho e_M}{\partial t} + \nabla \cdot (\rho \overrightarrow{u} e_M) + \nabla \cdot \left(\sum_s \rho_s \overrightarrow{U_s} e_{M,s} \right) = \nabla \cdot (\Lambda_M \nabla T_M) + \sum_{s,r,v,e} \frac{\epsilon_{M,s}^{r,v,e} \omega_s^{r,v,e}}{m_s} \tag{2.26}$$

where $T_M = T_{hr}$ for M = rotational and T_{ev} for M = (vibrational, electronic) in the two-temperature model. The mixture's thermal conductivity Λ_M can be expressed as:

$$\Lambda_M = n \sum_s \frac{x_s \hat{C}_{p,I,s}}{\sum_{j \neq e} (x_j / D_{sj})}. \tag{2.27}$$

Total Energy

The total energy equation is obtained by adding up the translational energy equation (Equation 2.6) derived using the Boltzmann equation with the equations for rotational, vibrational and electronic modes:

$$\begin{aligned} \frac{\partial \rho e}{\partial t} + \nabla \cdot (\rho \overrightarrow{u} h) + \nabla \cdot \left(\sum_s \rho_s \overrightarrow{U_s} h_s \right) &= \nabla \cdot [(\lambda_h + \lambda_r) \nabla T_{hr}] \\ + \nabla \cdot [(\lambda_v + \lambda_{el} + \lambda_e) \nabla T_{ev}] + \nabla \cdot (\overrightarrow{u} : \hat{\tau}) + \overrightarrow{J} \cdot \overrightarrow{E}. \end{aligned} \tag{2.28}$$

Electronic-vibrational Energy Equation

The energy in the electronic and vibrational modes of the heavy particles are assumed to be in equilibrium with the translation energy of the free electrons at a common temperature $T_{vib} = T_{elec} = T_{ev}$. Therefore, the electronic-vibrational energy of the mixture is given by:

$$\begin{aligned} \frac{\partial \rho e_{ev}}{\partial t} + \nabla \cdot (\rho \overrightarrow{u} e_{ev}) + \nabla \cdot \left(\sum_s \rho_s \overrightarrow{U_s} h_{ev,s} \right) &= \nabla \cdot [(\lambda_v + \lambda_{el} + \lambda_e) \nabla T_{ev}] \\ + \sum_{s \in mol.} \rho_s \frac{e^*_{V,s} - e_{V,s}}{\langle \tau_s \rangle} + 2 \rho_e \frac{3}{2} \overline{R} (T - T_{ev}) \sum_s \frac{\nu_{es}}{M_s} - \sum_{s \in ions} \dot{n}_{e,s} \hat{I}_s + \sum_{s \in mol.} C_s \dot{w}_s \hat{D}_s \end{aligned} \tag{2.29}$$

where $\overrightarrow{q_e}$ denotes the thermal conduction vector associated with the electronic and vibrational energy. The first term on the right defines the energy exchange (relaxation) between the vibrational and translational modes for molecular species due to collisions using the Landau-Teller model (Ω^{VT}). The second term denotes the energy exchange due to elastic collisions between electrons and heavy particles (Ω^{ET}); the third term represents the energy loss (summed over all ionized species) due to electron impact ionization (Ω^I). The last term gives the net change in vibrational energy due to

the dissociation of molecular species (Ω^{CV}).

2.3 Chemical Kinetic Model

Modeling reacting fluid flows that are in a state of thermal non-equilibrium requires calculating the chemical composition of the mixture and the population of internal energy modes. This information is also critical for accurately computing the transport and thermodynamic properties to close the system of governing equations. The energy relaxation processes for a two temperature model have already been defined in Equation 2.29. This section summarizes the modeling of chemical kinetics in the flow-field.

2.3.1 Local Thermodynamic Equilibrium (LTE)

A state of local thermodynamic equilibrium can be attained when the underlying chemistry for the given conditions is sufficiently fast with respect to the characteristic time of the flow. A simplified description for the mixture composition is then obtained by solving a system of non-linear algebraic equations [15, 17]. The solution obtained under LTE conditions is equivalent to solving the species conservation PDEs for chemical non-equilibrium in the limit of infinitely fast reactions. The classical LTE formulation assumes constant fraction of elements, allowing the mixture composition to be computed as a function of pressure and temperature throughout the flow-field. Flow solutions under the assumption of LTE have not been studied during the present work.

2.3.2 Chemical Non-equilibrium (CNEQ)

The capability to simulate chemical non-equilibrium conditions provides for a more complete description of the flow properties. The hydrodynamics equations include the effect of advection, diffusion and chemical processes and produce a flow-field with varying species concentration. The species continuity equations contain the mass production term due to chemical reactions for individual species which are computed using the law of mass-action. This net rate of mass production

of species s per unite volume can be defined as:

$$\omega_s = M_s \sum_{r=1}^{N_r} (\beta_{s,r} - \alpha_{s,r}) (R_{f,r} - R_{b,r}) \tag{2.30}$$

$$R_{f,r} = k_{f,r} \prod_s (\rho_s / M_s)^{\alpha_{s,r}} \tag{2.31}$$

$$R_{b,r} = k_{b,r} \prod_s (\rho_s / M_s)^{\beta_{s,r}} \tag{2.32}$$

where N_r represents the total number of reactions for a given species s. $\alpha_{s,r}$ and $\beta_{s,r}$ represent the stoichiometric coefficients for the reactants and products for the r^{th} reaction. The forward, $R_{f,r}$, and backward, $R_{b,r}$ reaction rates for reaction r are defined using Equations 2.31 and 2.32 respectively. $k_{f,r}$ and $k_{b,r}$ are the forward and backward reaction rate coefficients.

These calculations require accurate rate constants for all constitutive reactions for a given mixture. A multitude of databases for these rate constants with varying levels of uncertainity for high-temperature air are available in the literature. Therefore, the reliability of the rate data being used would have a strong bearing on the accuracy of any simulation involving chemical non-equilibrium. The present work uses the Park model [10, 11, 18] which gives rates values for the forward reaction rates. The backward reaction rates can then be calculated, according to the principle of detailed balance, by using the equilibrium constant [17].

2.3.3 Non-local Thermal Equilibrium (NLTE)

Multi-temperature models allow better representation of the physics by incorporating thermal non-equilibrium. The population of each internal energy mode for all species can then be calculated using a Maxwell-Boltzmann distribution at a specific temperature characterising a given mode (rotational T_r, vibrational T_v, or electronic temperature T_e). The chemical kinetics model is also modified to include NLTE effects. The macroscopic rate coefficients are computed for an empirical temperature value that is defined in terms of the different temperatures in the flow. The present work uses the Park model [11].

Park 2-T Model

The Park model [11] has been applied to a variety of flow problems and can be considered the standard model to account for thermo-chemical non-equilibrium effects. Reaction rate coefficients are computed for a geometric average of temperatures:

$$T_a = T_{hr}^{1-q_i} \, T_{ev}^{q_i} \tag{2.33}$$

where q_i is defined as the vibration-dissociation coupling term for the i^{th} reaction. The value of q_i is usually set to 0.5 in the absence of reaction specific data. The current study uses different values of this parameter for Nitrogen and Oxygen dissociation due to the different dynamics of dissociation for the two molecules.

Vibration-Chemistry Coupling

Chemical reactions involving molecules affect the total vibrational energy present in the mixture. Therefore, an additional source term arising from chemical non-equilibrium is introduced in the electronic-vibrational energy equation (Equation 2.29). Candler and MacCormack [19] have developed a simplified formulation for the change in vibrational energy:

$$\Omega^{CV} = \sum_{s \in mol.} C_s \, \dot{w}_s \, \hat{D}_s \tag{2.34}$$

where $\hat{D}_s$ denotes the dissociation energy per unit mass for a given molecular species s. C_s represents the fraction of dissociation energy lost as vibrational energy during the dissociation of s. The exact amount of energy that is lost due to a specific chemical reaction can be determined through a state-to-state (or collisional radiative models) approach [20, 21, 22, 23, 24, 25]. However, this becomes computationally prohibitive for complex CFD applications due to the large number of equations and individual kinetic processes.

The different dissociation models that have been described in literature can be classified as 1) *preferential* 2) *non-preferential*. The *preferential* models are based on the assumption that

dissociation occurs from the higher vibrational quantum states and molecules in the lower states must be excited to higher states (*ladder climb*) before they dissociate. The present work uses a *non-preferential* model, which assigns equal probability of dissociation to all quantum states of a given molecule. This assumption becomes increasingly valid as the free-stream kinetic energy approaches the dissociation energy of molecules, resulting in dissociation at all levels without the *ladder climb* process. The constant C_s is assumed to be equal to one for the non-preferential model and would assume larger values for preferential dissociation.

2.4 Transport Properties

The transport properties module in the original version of Mutation++ uses the Chapman-Enskog method [16, 26] to obtain transport fluxes as linear functions of gradients of flow variables with the transport coefficients appearing as constants of proportionality. Although the Chapman-Enskog method is formulated on rigorous kinetic theory, it is computationally expensive and challenging to implement efficiently. The complicated expressions also lend themselves poorly to improving the overall stability of the simulation framework. Consequently, non-physical transport coefficients can be obtained for a perfectly plausible set of state values at a given point in the flow field, severely retarding solver capabilities.

This complicated approach has been dropped in favor of simplified expressions for different properties outlined by Gnoffo et al. [10] for an ionized mixture. This formulation is very similar to the one obtained by Lee [27] and expands upon the work of Yos [28] to include the effects of thermal non-equilibrium. The use of Gnoffo's techniques for modeling transport properties has improved reliability and reduced computing costs, with negligible effect on the accuracy of the solution for the flow conditions being studied during the present work.

2.4.1 Collision Integrals

Collision integrals, $\overline{\Omega}_{sr}^{(l,m)}$ can be viewed as generalized cross-sections describing the interactions between s and r, with the indices l and m denoting the type of collision being considered. The

collision integrals for heavy particles are computed using the heavy-particle translational temperature, T_{hr}, while collisions integrals for interactions involving electrons are based on the electron / electronic-vibrational temperature, T_{ev}. The collision integrals are computed using curve-fitted expressions as functions of temperature, generated from tabulated data in literature [15]. Two modified collision integrals that are used extensively in all subsequent property calculations are as follows:

$$\Delta_{sr}^{(1)}(T) = \frac{8}{3}\left[\frac{2M_sM_r}{\pi R_u T(M_s+M_r)}\right]^{1/2}\overline{\Omega}_{sr}^{(1,1)} \tag{2.35}$$

$$\Delta_{sr}^{(2)}(T) = \frac{16}{5}\left[\frac{2M_sM_r}{\pi R_u T(M_s+M_r)}\right]^{1/2}\overline{\Omega}_{sr}^{(2,2)} \tag{2.36}$$

2.4.2 Heavy Particle Transport Properties

The molar concentration of species s, γ_s, is defined as

$$\gamma_s = \frac{\rho_s}{\rho M_s} \tag{2.37}$$

The mixture viscosity can then be computed using the following expression by adding up the contributions of all heavy-particle species:

$$\mu = \sum_{s\in heavy}\frac{m_s\gamma_s}{\sum\limits_{r\in heavy}\gamma_r\Delta_{sr}^{(2)}(T_{hr})+\gamma_e\Delta_{sr}^{(2)}(T_{ev})} + \frac{m_e\gamma_e}{\sum\limits_r\gamma_r\Delta_{er}^{(2)}(T_{ev})} \tag{2.38}$$

The translational energy thermal conductivity of heavy particles, λ_t, is computed by the following expression

$$\lambda_t = \frac{15}{4}k\sum_{s\in heavy}\frac{\gamma_s}{\sum\limits_{r\in heavy}a_{sr}\gamma_r\Delta_{sr}^{(2)}(T_{hr})+3.54\gamma_e\Delta_{se}^{(2)}(T_{ev})} \tag{2.39}$$

where a_{sr} is defined by

$$a_{sr} = 1 + \frac{[1-(m_s/m_r)][0.45 - 2.54(m_s/m_r)]}{[1+(m_s/m_r)]^2} \tag{2.40}$$

The molecular rotational modes are considered to be fully excited and the thermal conductivity associated with rotational energy, λ_r, is expressed as

$$\lambda_r = k \sum_{s \in mol.} \frac{\gamma_s}{\sum\limits_{r \in heavy} \gamma_r \Delta^{(1)}_{sr}(T_{hr}) + \gamma_e \Delta^{(1)}_{se}(T_{hr})} \tag{2.41}$$

The vibrational thermal conductivity λ_v is assumed to be equal to the rotational thermal conductivity λ_r. Therefore,

$$\lambda_v = \lambda_r \tag{2.42}$$

The binary diffusion coefficient for a pair of heavy particles s and r is given by

$$D_{sr} = \frac{k\,T_{hr}}{p\Delta^{(1)}_{sr}(T_{hr})} \tag{2.43}$$

The binary diffusion coefficient when one of the species is a free electron is:

$$D_{er} = \frac{k\,T_{ev}}{p\Delta^{(1)}_{er}(T_{ev})} \tag{2.44}$$

The effective diffusion for species s in the mixture, D_s, is computed using the following mixture average rule:

$$D_s = \frac{1 - x_s}{\sum\limits_{r \neq s} x_r / D_{sr}} \tag{2.45}$$

The diffusion of ions and electrons is coupled due to the electron pressure gradient term that

induces an electric field. Thus, a partially ionized gas can be described with the ambipolar diffusion coefficient D^a_{ion}, where

$$D^a_{ion} = 2D_{ion} \tag{2.46}$$

2.4.3 Electron Particle Transport Properties

The thermal conductivity of the free electron, λ_e, is given by

$$\lambda_e = \frac{15}{4} k \frac{\gamma_e}{\sum_r 1.45 \gamma_r \Delta^{(2)}_{er}(T_{ev})} \tag{2.47}$$

The diffusion velocity of each ion is calculated by treating it as the only ionic species present in the gaseous mixture. Developing the ambipolar constraint further, the effective diffusion coefficient of electrons, D_e, is computed by equating the diffusion velocity of electrons with the diffusion velocity of ions. Thus, D_e can then be calculated using:

$$D_e = m_e \frac{\sum_{s \in ions} D^a_s \gamma_s}{\sum_{s \in ions} m_s \gamma_s} \tag{2.48}$$

The electrical conductivity is expressed using a single non-vanishing Sonine polynomial:

$$\sigma = \frac{3 n_e q_e^2 \left(8 k_B T_{ev} / \pi m_e\right)^{-1/2}}{4 m_e \sum_{j \neq e} n_j \overline{\Omega}^{(1,1)}_{ej}} \tag{2.49}$$

2.4.4 Comparative Analysis Between Transport Property Formulations

A comparison with results obtained through the Chapman-Enskog method combined with the Eucken correction is essential for establishing the suitability of transport property models used by Gnoffo et al.[10]. A two-fold analysis has been carried out: 1) Comparison for different transport properties for a zero-dimensional reaction mixture comprising of LTE Air-11 at 1 atm. 2) Evaluation of stagnation line properties for two-dimensional hypersonic flow over a cylinder.

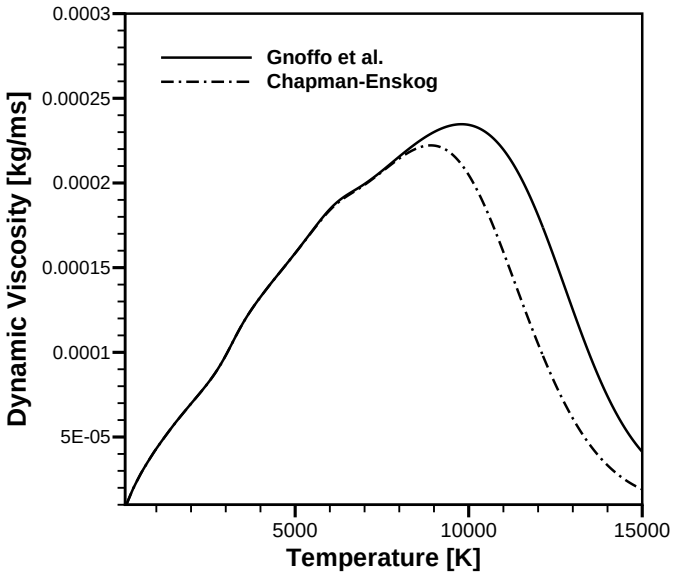

Figure 2.1: Calculated values of viscosity for LTE Air-11 at 1 atm

Figure 2.1 shows the temperature variation in viscosity values for LTE Air-11 at 1 atm. The simplified mixture rules for viscosity presented in [10] demonstrate good accuracy, with significant deviations occurring only at temperatures in excess of 10000 K. Figure 2.2 presents a comparison between different components of the mixture thermal conductivity for the same zero-dimensional test case. Translational thermal conductivity of both heavy particles and electrons are in excellent agreement over a wide temperature range. The contributions of rotational and vibrational modes match up as well. Electronic thermal conductivity is not modeled using mixture rules outlined by Gnoffo et al. and is assigned a value equal to zero. Thus, despite values of individual components differing for the two approaches, the total thermal conductivity can be calculated to a high degree of accuracy up to 10000 K, using mixture rules.

The impact of transport property models on flow solutions for actual CFD applications has been studied by analyzing the stagnation line properties obtained for a two-dimensional flow over

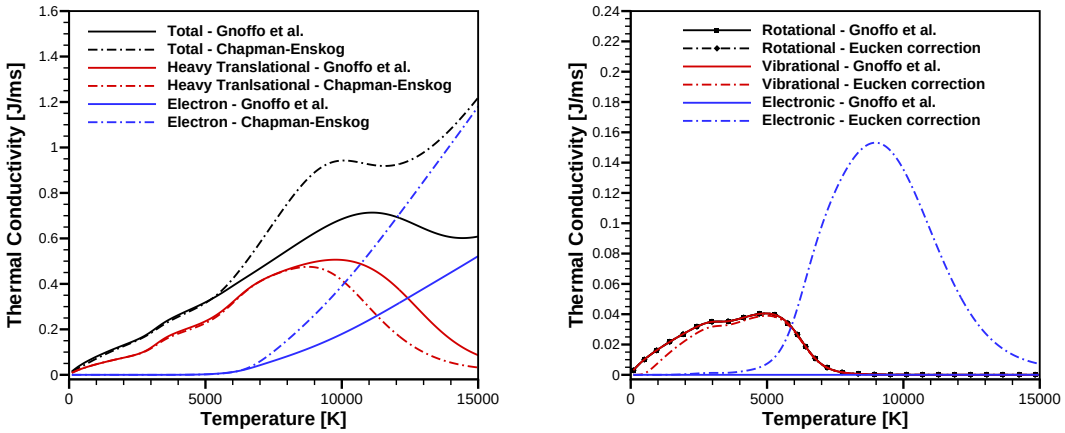

(a) Total and translational thermal conductivity

(b) Thermal conductivity due to internal energy modes

Figure 2.2: Calculated values of thermal conductivity for LTE Air-11 at 1 atm

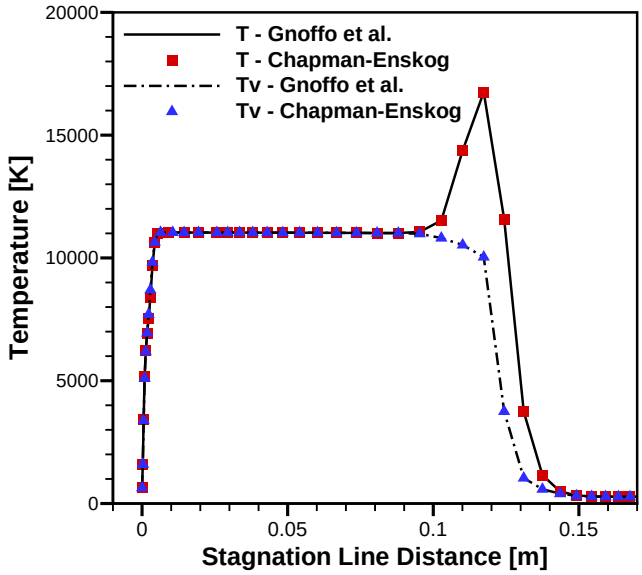

Figure 2.3: Temperature distribution along stagnation line for hypersonic flow over cylinder using different transport property models

a cylinder of radius, $R = 0.8\ m$. The following free-stream variables are used for this analysis:

$$\begin{aligned} u_\infty &= 10480 \text{ m/s} \\ \rho_\infty &= 7.80\times10^{-4} \text{ kg/m}^3 \\ T_\infty &= 276 \text{ K} \end{aligned}$$

A strong bow shock is formed upstream to the cylinder which produces strong thermal and chemical non-equilibrium effects in its vicinity. Figure 2.3 illustrates the stagnation line temperature distribution obtained using mixture rules and Chapman-Enskog formulations. Results obtained using both methods are in excellent agreement. Discrepancies in transport property values at very high temperatures are largely local and have no discernible impact on the macroscopic distribution of flow properties. Thus, the use of simplified mixture rules provides clear cost and stability advantages without compromising the accuracy of flow-field solutions.

2.5 Turbulence Modeling

The computational cost of resolving all the scales of turbulence for high enthalpy flows in thermochemical non-equilibrium is prohibitive due to the size of the system of governing equations (Equations 2.22 – 2.29) and the complex property models required for defining the problem. Consequently, Equations 2.22 – 2.29 are density weighted time averaged to obtain the Favre-averaged Navier-Stokes (FANS) equations. The averaging over non-linear terms requires a turbulence model to close the system of equations. The concept of eddy viscosity is used to account for the effects of turbulence. The system of equations remains unchanged but transport properties are modified to include the

effect of "eddy" transport variables in the following manner:

$$\begin{aligned} \mu &\rightarrow \mu + \mu_t \\ D &\rightarrow D + D_t \\ k &\rightarrow k + k_t \\ \lambda &\rightarrow \lambda + \lambda_t \\ \lambda_{ev} &\rightarrow \lambda_{ev} + \lambda_{ev,t} \end{aligned}$$

Eddy viscosity, μ_t, is used to calculate eddy mass diffusivity, D_t, and thermal conductivities, λ_t and $\lambda_{ev,t}$:

$$\begin{aligned} D_t &= \frac{\mu_t}{\rho\, Sc_t} \\ k_t &= \frac{\mu_t\, C_p}{Pr_t} \\ \lambda_{ev,t} &= \eta\, \mu_t\, C_v^{ev} \end{aligned} \tag{2.50}$$

where Sc_t, Pr_t, and η represent model parameters. The eddy viscosity is computed using the Spalart-Allmaras (SA) one-equation model [29]. This requires adding an additional transport equation for the working variable ν_{SA}. μ_t is then obtained from ν_{SA} by solving a set of algebraic closure relationships. The extra transport equation is as follows:

$$\begin{aligned} \frac{\partial \rho \nu_{SA}}{\partial t} + \nabla \cdot (\rho \overrightarrow{u} \nu_{SA}) &= c_{b1}\, S_{SA}\, \rho\, \nu_{SA} - c_{w1} f_w \rho \left(\frac{\nu_{SA}}{d}\right)^2 \\ &+ \frac{1}{Pr_t} \cdot [(\mu + \rho \nu_{SA}\, \nabla \nu_{SA}] + \frac{c_{b2}}{Pr_t}\, \rho\, \nabla \nu_{SA} \cdot \nabla \nu_{SA} \end{aligned} \tag{2.51}$$

The algebraic closure relationships for the SA model are:

$$\mu_t = \rho\,\nu_{SA}\,f_{v1} \tag{2.52}$$

$$f_{v1} = \frac{\chi^3}{\chi^3 + c_{v1}^3} \tag{2.53}$$

$$f_{v2} = 1 - \frac{\chi}{1 + \chi, f_{v1}} \tag{2.54}$$

$$\chi = \frac{\nu_{SA}}{\nu} \tag{2.55}$$

$$f_w = g\left(\frac{1 + c_{w3}^6}{g^6 + c_{w3}^6}\right)^{1/6} \tag{2.56}$$

$$g = r + c_{w2}\,(r^6 - r) \tag{2.57}$$

$$r = \frac{\nu_{SA}}{S_{SA}\,\kappa^2\,d^2} \tag{2.58}$$

A slightly modified form of the final closure function, S_{SA}, has been used in the present work. The original formulation for S_{SA} is:

$$S_{SA} = \Omega + \frac{\nu_{SA}}{\kappa^2 d^2}\,f_{v2} \tag{2.59}$$

where Ω represents the vorticity magnitude. Equation 2.59 is modified to ensure S_{SA} is always greater than zero. The final form is:

$$S_{SA} = \Omega + S_m \tag{2.60}$$

S_m is defined in the following manner:

$$S_m = \begin{cases} S_{m0}, & \text{if } S_{m0} \geq -c_{v2}\Omega \\ \frac{\Omega\left(c_{v2}^2 + c_{v3}\,S_{m0}\right)}{((c_{v3} - 2c_{v2})\Omega - S_{m0})}, & \textit{otherwise.} \end{cases} \tag{2.61}$$

$$S_{m0} = \frac{\nu_{SA}}{\kappa^2\,d^2}\,f_{v2} \tag{2.62}$$

Chapter 3

Numerical Method

3.1 System Form of Equations

Equations 2.22 – 2.29 can be written in the conservative form in the following manner:

$$\frac{\partial \mathbf{U}}{\partial t} + \frac{\partial \mathbf{F}_i}{\partial x_i} = \frac{\partial \mathbf{G}_i}{\partial x_i} + \dot{\mathcal{S}} \tag{3.1}$$

where $\mathbf{U} = [\ \rho_s, \rho u_j, \rho e, \rho e_{ev}, \rho \nu_{SA}\ ]^T$ is the vector of conservative variables representing species density, cartesian components of momentum per volume, total energy per unit volume, electronic-vibrational energy per unit volume. $\mathbf{F}_i$ and $\mathbf{G}_i$ are the inviscid and viscous fluxes, respectively, in the i^{th} direction. The vibronic energy equation is omitted while modeling flows in thermal equilibrium. The Spalart-Allmaras working variable, ν_{SA}, is added for the turbulent case.

The second term on the left hand side of Equation 3.1, which is the divergence of the inviscid flux vector, can be described using the inviscid flux Jacobian, $\mathbf{A}_i = \partial \mathbf{F}_i \,/\, \partial x_i$, in terms of the $\mathbf{U}$ vector:

$$\frac{\partial \mathbf{F}_i}{\partial x_i} = \frac{\partial \mathbf{F}_i}{\partial \mathbf{U}} \frac{\partial \mathbf{U}}{\partial x_i} = \mathbf{A}_i \frac{\partial \mathbf{U}}{\partial x_i} \tag{3.2}$$

The inviscid flux vector is further split into convective (contributions stemming from the fluid velocity) and pressure contributions. Analogous to the previous expression for the inviscid fluxes,

a description employing the inviscid flux Jacobian is also obtained for this split formulation:

$$\begin{aligned} \mathbf{F}_i &= \mathbf{F}_i^C + \mathbf{F}_i^P \qquad (3.3) \\ \frac{\partial \mathbf{F}_i}{\partial x_i} &= \frac{\partial \mathbf{F}_i^C}{\partial x_i} + \frac{\partial \mathbf{F}_i^P}{\partial x_i} \\ &= \mathbf{A}_i^C \frac{\partial \mathbf{U}}{\partial x_i} + \mathbf{A}_i^P \frac{\partial \mathbf{U}}{\partial x_i} \qquad (3.4) \end{aligned}$$

This form for the invsicid flux vector is unconventional but is extremely useful for implementing boundary conditions. Similarly, the viscous flux vector $\mathbf{G}_i$ can also be written as:

$$\frac{\partial \mathbf{G}_i}{\partial x_i} = \frac{\partial}{\partial x_i}\left(\mathbf{K}_{ij}\frac{\partial \mathbf{U}}{\partial x_j}\right) \qquad (3.5)$$

where $\mathbf{K}_{ij}$ is the diffusivity matrix. The matrices $\mathbf{A}_i$ and $\mathbf{K}_{ij}$ can be expressed in terms of the independent variables $\mathbf{U}$. The strong form of the second order system, that is the basis for all further developments, is then obtained from Equations 3.1, 3.4, and 3.5.

$$\frac{\partial \mathbf{U}}{\partial t} + \left(\mathbf{A}_i^C + \mathbf{A}_i^P\right)\frac{\partial \mathbf{U}}{\partial x_i} = \frac{\partial}{\partial x_i}\left(\mathbf{K}_{ij}\frac{\partial \mathbf{U}}{\partial x_j}\right) + \dot{\mathcal{S}} \qquad (3.6)$$

In the case of inviscid flows, Equation 3.6 reduces to the first-order, hyperbolic reacting Euler equations.

3.2 Weak Formulation

3.2.1 Galerkin Weak Statement

The weak form of the system of equations described in 3.6 can be formulated by multiplying by an appropriate set of test functions $\mathbf{W}$ and then integrating over the entire domain Ω. The convective components of the inviscid flux and the viscous terms can be integrated by parts to obtain the final

form of the weak statement:

$$\int_{\Omega} \left[\mathbf{W} \,.\, \left(\frac{\partial \mathbf{U}}{\partial t} + \mathbf{A}_i^P \, \frac{\partial \mathbf{U}}{\partial x_i} - \dot{\mathcal{S}} \right) + \frac{\partial \mathbf{W}}{\partial x_i} \,.\, \left(\mathbf{K}_{ij} \, \frac{\partial \mathbf{U}}{\partial x_j} - \mathbf{A}_i^C \, \frac{\partial \mathbf{U}}{\partial x_i} \right) \right] d\Omega \\ - \int_{\Gamma} \mathbf{W} \,.\, (\mathbf{g} - \mathbf{f}) d\Gamma \, = \, 0 \tag{3.7}$$

where $\mathbf{U}$ satisfies the essential boundary and initial conditions for all $\mathbf{W}$ in an appropriate function space. The last term is the integral of the normal components of the viscous fluxes, $\mathbf{g} = \mathbf{G} \,.\, \hat{n}$, and the convective inviscid fluxes, $\mathbf{f} = \mathbf{F}^C \,.\, \hat{n}$, on the boundary Γ with unit normal $\hat{n}$.

3.2.2 Stabilized Upwind Formulation

The standard Galerkin formulation employed in Equation 3.7 is unstable and can generate non-physical oscillations in regions of steep solution gradients or strong convection. This oscillatory behavior for convection dominated flows can persist even after including the effects of vicosity. This is a well documented phenomenon afflicting standard Galerkin formulations (or equivalent central difference schemes on a structured grid), and occurs because they produce a difference stencil whose solutions admit oscillatory behavior [30, 31]. This instability can also stem from inadequate spatial resolution for some class of flows and can be resolved using a sufficiently fine mesh. An example of such problems are low speed incompressible flows where there is an approximate balance between the convective and diffusive length scales. Unfortunately, such balance is seldom observed for compressible flows. Additionally, Euler equations have no diffusion terms, rendering the standard Galerkin formulation ill-suited for modeling inviscid flows, irrespective of the mesh resolution.

Several techniques have been proposed that seek to remedy the stability issues encountered by the standard Galerkin formulation. The Lax-Wendroff finite difference scheme, when applied to a finite element problem, results in the Taylor-Galerkin scheme. The Taylor-Galerkin scheme uses a second-order Taylor series in time and an exchange of spatial and temporal differentiation while discretizing Equation 3.1. This creates a second-order term that can be viewed as a stabilizing diffusion. The Taylor-Galerkin scheme has recently been used to model hypersonic non-equilibrium flows, highlighting its applicability to the class of flows being investigated in the current study [32].

Carey et al. have used a different approach – the Least-Squares finite element method. In this method, the test function $\mathbf{W}$ in Equation 3.7 is substituted with the variation of the residual of governing equations [33, 34] and results in the least square minimization of the residual. Least-squares minimization can be combined with the Galerkin weak statement to obtain the so-called Galerkin/least-squares scheme.

An upward bias can be added to the test function $\mathbf{W}$ for improving stability through numerical dissipation due to upwind differencing. The directed streamline-upwind Petrov/Galerkin (SUPG) formulation provides for a stabilization mechanism in convection dominated flows and reduces cross-wind dissipation in two or three dimensions. The modified test function with suitable upwind-biasing is defined as follows:

$$\hat{\mathbf{W}} \;=\; \mathbf{W} \;+\; \tau_{SUPG}\, \mathbf{A}_i\, \frac{\partial \mathbf{W}}{\partial x_i} \tag{3.8}$$

where $\mathbf{W}$ is the unbiased standard Galerkin test function and τ_{SUPG} is the stabilization matrix that introduces the minimum amount of diffusion required for stabilizing the scheme.

3.2.3 Streamline-Upwind Stabilization Matrix

The stabilization matrix, τ_{SUPG}, employed by FIN-S is based on the work of Erwin et al. [35].

$$\tau_{SUPG}^{-1} \quad = \quad \sum_{i=nodes} \left(\left| \frac{\partial \phi_i}{\partial x_j}\, \mathbf{A}_j \right| \;+\; \frac{\partial \phi_i}{\partial x_j}\, \mathbf{K}_{jk}\, \frac{\partial \phi_i}{\partial x_k} \right) \tag{3.9}$$

where ϕ_i is the shape function associated with the i^{th} node in the finite element. This formulation does not depend on the heuristic definition of a flow-aligned length scale and has been extensively used for a wide variety of applications. τ_{SUPG} can be computed by expressing the absolute value matrix on the right hand side of Equation 3.9 as:

$$\left| \frac{\partial \phi_i}{\partial x_j}\, \mathbf{A}_j \right| \quad = \quad \mathbf{R}\, |\mathbf{\Lambda}| \mathbf{R}^{-1} \tag{3.10}$$

where $\mathbf{\Lambda}$ represents the diagonal matrix containing the eigen-values and $\mathbf{R}$ represents the right eigen vector matrix of the inviscid Jacobian. Analytic expressions of $\mathbf{\Lambda}$ and $\mathbf{R}$, obtained for laminar flow

in thermal non-equilibrium, have been used. The matrix $\frac{\partial \phi_i}{\partial x_j}\,\mathbf{A}_j$ can be visualized as the component of the inviscid flux in the direction defined by the shape function gradients. Also

$$\frac{\partial \phi_i}{\partial x_j}\,\mathbf{A}_j \;=\; \mathbf{R}\,\mathbf{\Lambda}\mathbf{R}^{-1} \tag{3.11}$$

Therefore, the inviscid contribution in Equation 3.10 can be calculated using $|\Lambda|$ obtained from Equation 3.11.

3.2.4 Discontinuity Capturing Operator

The schemes that have been discussed so far seek to address instabilities caused by strong convective flows that plague the standard Galerkin formulation. Supersonic flows with strong shock waves would require additional stabilizing schemes to eliminate non-physical oscillations stemming from strong gradients. This is achieved through a discontinuity capturing operator, ν_{DCO}, which introduces isotropic artificial dissipation locally and allows the shock to be captured in a thin region comprising of a few cells. ν_{DCO} depends on gradients in the computational space encapsulated in the contravariant metric tensor

$$g^{ij} \;=\; \frac{\partial x_i}{\partial \xi k}\,\frac{\partial x_j}{\partial \xi k} \tag{3.12}$$

The discontinuity operator for a system of conservative variables has been devised by LeBeau and Tezduyar [36, 37, 38], and are a modified form of the original function used by Hughes et al. for entropy variables [39]. The present work employs the following form of this operator:

$$\nu_{DCO} \;=\; \left[\frac{\left\| \frac{\partial \mathbf{U}}{\partial t} + \mathbf{A}_i^P\,\frac{\partial \mathbf{U}}{\partial x_i} - \frac{\partial}{\partial x_i}\left(\mathbf{K}_{ij}\,\frac{\partial \mathbf{U}}{\partial x_j}\right)\right\|^2_{\mathbf{A}_0^{-1}}}{(\Delta \mathbf{U}_h)^T\,\mathbf{A}_0^{-1}\,\Delta \mathbf{U}_h \;+\; g^{ij}\left(\frac{\partial \mathbf{U}_h}{\partial x_i}\right)^T\,\mathbf{A}_0^{-1}\,\frac{\partial \mathbf{U}_h}{\partial x_i}}\right]^{1/2} \tag{3.13}$$

where $\mathbf{A}_0^{-1}$ is the mapping from conservation to entropy variables. $\Delta \mathbf{U}_h$ is the change in $\mathbf{U}_h$ over

one time step and can be calculated as:

$$\Delta \mathbf{U}_h = \frac{\partial \mathbf{U}_h}{\partial t} \Delta t \tag{3.14}$$

This approach of combining streamline upwinding and shock capturing to obtain stable solutions within a finite element formulation is similar to the upwinding and limiting encountered in total-variation-diminishing (TVD) finite difference and finite volume schemes. TVD schemes use upwinding for the inviscid flux terms to improve stability in convection-dominated flows while flux or slope-limiters impose monotonicity in the presence of strong shocks. The discontinuity operator outlined in the present work performs similarly to limiters and attempts to restore monotonicity in regions of large gradients.

3.2.5 Boundary Conditions

For the class of flows investigated in the present work, the system of Navier-Stokes equations is a mixed parabolic-hyperbolic set of partial differential equations. The different boundary conditions that are relevant for such flows are as follows:

Supersonic Inflow

In the case of supersonic inflow, all characteristics point towards the domain, and therefore, each variable can be imposed as an essential boundary condition. Freestream density, velocity, and temperature are the usual prescribed variables for aerothermodynamic studies.

Supersonic Outflow

At boundaries with supersonic outflow, the flow state is defined entirely by the information from inside the domain. In case of viscous flows, it is important that the viscous terms, obtained after integrating Equation 3.7 by parts, are retained in the boundary integral.

Viscous Walls

A no-slip and no-penetration boundary condition, $\mathbf{u} = \rho\,\mathbf{u} = 0$ is imposed as a Dirichlet condition on viscous walls. Additionally, the wall is assumed to be in thermal equilibrium with $T = T_v$. This is implemented by linearizing the residual equation $\mathcal{R}_{\rho e_{ev},\,wall} = (T - T_v)$ with respect to the conservative variables and imposing the resultant value as a Dirichlet constraint [40].

1. Isothermal Walls: $T = T_{wall}$ is ensured through an additional Dirichlet constraint obtained by linearizing $\mathcal{R}_{\rho e,\,wall} = (T - T_{wall})$, with respect to the conservative variables.

2. Convecting Walls: This condition provides for a more realistic description of the heating phenomenon at the wall. The numerical stiffness of the flow problem, compared to a case with isothermal boundary, is also reduced, especially in the presence of large temperature gradients near the wall region. The energy flux on the wall surface is defined as:

$$\mathbf{q}\,.\,\hat{\mathbf{n}} = -h_w\,(T - T_{wall}) \tag{3.15}$$

3. Mass injection: The test gas is injected through the walls of the constrictor in segmented arc heaters. Therefore, it is necessary to incorporate a boundary condition that reproduces this feature in order to obtain accurate simulations. A constant mass flux is imposed on the wall surface. Temperature can be specified in the manner of either isothermal or convecting wall condition. This allows the wall normal velocity to be computed which is necessary for specifying the momentum flux on the boundary.

Characteristic-based boundaries

In case of subsonic inlet and subsonic outlet, the state of the system at the boundary, $\mathbf{U}$, is computed by solving the characteristic equations, using the reference state $\mathbf{U}_\infty$ and solution on the boundary $\mathbf{U}_B$. The conserved variables can be transformed into the characteristic variables in the following manner:

$$\delta\hat{\mathbf{U}} = \frac{\partial\hat{\mathbf{U}}}{\partial\mathbf{U}}\,\delta\mathbf{U} = \mathbf{M}^{-1}\,\delta\mathbf{U} \tag{3.16}$$

where $\delta\mathbf{U}$ is the perturbed value of the conserved variables and $\delta\hat{\mathbf{U}}$ is the corresponding vector of characteristic variables. $\mathbf{M}^{-1}$ is the transformation matrix formed by the left eigenvectors obtained from Eigen decomposition of the inviscid flux in a specified direction.

The correct state at the boundary can be obtained through a series of iterations, by computing $\delta\hat{\mathbf{U}}$ from the incoming and the outgoing characteristics that are consistent with $\mathbf{U}_\infty$ and $\mathbf{U}_B$. In case of negative eigenvalues information flows into the domain from the farfield, hence components from $\delta\hat{\mathbf{U}}^-$ are used. Conversely, for positive eigenvalues, information is exiting the domain, therefore, components from $\delta\hat{\mathbf{U}}^+$ are used. The task of selecting the proper values from $\delta\hat{\mathbf{U}}^+$ and $\delta\hat{\mathbf{U}}^-$ is carried out by the **combine** () operator. Characteristic boundary conditions are computed using the following algorithm:

1. Assume $\mathbf{U} = \mathbf{U}_B$ as the initial guess
2. **do**
3. Calculate the transformation matrix $\mathbf{M}^{-1} = \mathbf{M}^{-1}(\mathbf{U})$
4. Define $\delta\hat{\mathbf{U}}^+ = \mathbf{U} - \mathbf{U}_B$
5. Define $\delta\hat{\mathbf{U}}^- = \mathbf{U} - \mathbf{U}_\infty$
6. Combine the two characteristic incriments: $\delta\hat{\mathbf{U}} = \mathbf{combine}\,(\delta\hat{\mathbf{U}}^+, \delta\hat{\mathbf{U}}^-)$, where each component depends on the sign of the associated eigenvalue.
7. Compute incrimental value $\mathbf{M}^{-1}\,\delta\mathbf{U} \equiv -r = \delta\hat{\mathbf{U}}$
8. Update state $\mathbf{U} \longleftarrow \mathbf{U} + \delta\mathbf{U}$
9. **while** $||\delta\mathbf{U}||_\infty > \epsilon_{it}$
10. Compute inviscid flux on the boundary and apply to weak statement.

Spalart-Allmaras turbulence model

$\nu_{SA} = 0$ is imposed at the wall. A value of $\nu_{SA} = 5\,\nu$ (where ν is the kinematic viscosity in the freestream) is used at the inlet to obtain fully turbulent flows.

3.3 Finite Element Formulation

An approximate finite element formulation is obtained upon discretizing the weak form generated through the test functions, $\mathbf{W}_h$ by introducing the approximate solution, $\mathbf{U}_h$, and the corresponding shape functions.

$$\sum_{e=1}^{n_{el}} \int_{\Omega_e} \left[\mathbf{W}_h \cdot \left(\frac{\partial \mathbf{U}_h}{\partial t} + \mathbf{A}_i^P \frac{\partial \mathbf{U}_h}{\partial x_i} - \dot{\mathcal{S}}_\mathbf{h} \right) + \frac{\partial \mathbf{W}_h}{\partial x_i} \cdot \left(\mathbf{K}_{ij} \frac{\partial \mathbf{U}_h}{\partial x_j} - \mathbf{A}_i^C \frac{\partial \mathbf{U}_h}{\partial x_i} \right) \right] d\Omega$$
$$+ \sum_{e=1}^{n_{el}} \int_{\Omega_e} \tau_{SUPG} \frac{\partial \mathbf{W}_h}{\partial x_k} \cdot \mathbf{A}_k \left[\frac{\partial \mathbf{U}_h}{\partial t} + \mathbf{A}_i \frac{\partial \mathbf{U}_h}{\partial x_i} - \frac{\partial}{\partial x_i} \left(\mathbf{K}_{ij} \frac{\partial \mathbf{U}_h}{\partial x_j} \right) - \dot{\mathcal{S}}_\mathbf{h} \right] d\Omega$$
$$\sum_{e=1}^{n_{el}} \int_{\Omega_e} \nu_{DCO} \left(\frac{\partial \mathbf{W}_h}{\partial x_i} \cdot g^{ij} \frac{\partial \mathbf{U}_h}{\partial x_j} \right) d\Omega - \sum_{e=1}^{n_{el}} \int_{\Gamma_e} \mathbf{W}_h \cdot (\mathbf{g}_h - \mathbf{f}_h) \, d\Gamma = 0 \qquad (3.17)$$

$\mathbf{U}_h(\mathbf{x}, t)$ and $\mathbf{F}_i(\mathbf{x}, t)$ can be expressed as a linear combination of the nodal solution values, $\mathbf{U}_h(\mathbf{x}_j, t)$, and nodal inviscid flux components, $\mathbf{F}_i(\mathbf{x}_j, t) = \mathbf{A}_i(\mathbf{U}_h(\mathbf{x}_j, t))\,\mathbf{U}_h(\mathbf{x}_j, t)$, respectively, using the finite element basis functions.

$$\mathbf{U}_h(\mathbf{x}, t) = \sum_j \mathcal{N}_j(\mathbf{x})\, \mathbf{U}_h(\mathbf{x}_j, t) \qquad (3.18)$$

$$\mathbf{F}_i(\mathbf{x}, t) = \sum_j \mathcal{N}_j(\mathbf{x})\, \mathbf{F}_i(\mathbf{x}_j, t) \qquad (3.19)$$

$\mathcal{N}_j$ consists of a set of standard piecewise linear Lagrangian basis polynomials, which results in a second–order accurate scheme. Previous research on the application of the finite element method to the compressible Navier-Stokes equations indicates that the current scheme can easily be extended to higher-order spatial discretization, in the absence of shocks, by using a higher order finite element basis [41]. The manner in which $\mathbf{F}_i$ is discretized, as described in Equation 3.19, has shown to improve the stability of the SUPG method in the presence of strong shocks [3].

3.4 Solution Methodology

The set of equations defined in 3.17 form a transient, tightly coupled nonlinear system whose solution are the unknown nodal values, $\mathbf{U}_h(\mathbf{x}_j, t)$. Even in the case of steady state problems, time marching is carried out to reach the steady solution by integrating 3.17 in time. This approach is especially appropriate for compressible flows with strong shocks, since regions with strong gradients result in an extremely small zone of attraction for non-linear implicit scheme such as Newton's method [42, 43]. The transient system can be solved using two kinds of methods: explicit and implicit. The h-dependence of δ_t for explicit methods, which can impede attempts to locally resolve flow physics at smaller scales (by reducing h), renders them unsuitable for the present work. Conversely, the improved stability offered by implicit methods comes at high computational costs associated with solving a non-linear implicit system at each time step. Preconditioned Krylov subspace iterative methods are well suited for overcoming this constraint and can also be implemented in a parallel framework [44].

The METIS unstructured graph partitioning library [45] has been used to achieve non-overlapping domain decomposition with a unique set of elements assigned to each processor used in the simulation. This approach allows each processor to compute the system matrix contributions of only the local elements. These are then aggregated into a sparse matrix data structure and used by the Krylov subspace solver to obtain an approximate solution to the linear system [46, 5, 47].

A backward difference scheme has been use to discretize the semi-discrete set of equations in 3.17. A Taylor series expansion about $\mathbf{U}_h(t_{n+1}) = \mathbf{U}_{n+1}$ is used to obtain both first and second order accurate in time formulations.

$$\begin{aligned}
\mathbf{U}_n &= \mathbf{U}_{n+1} + \frac{\partial \mathbf{U}_{n+1}}{\partial t}(t_n - t_{n+1}) + \frac{\partial^2 \mathbf{U}_{n+1}}{\partial t^2}\frac{(t_n - t_{n+1})^2}{2} + \mathcal{O}\left((t_n - t_{n+1})^3\right) \\
\mathbf{U}_{n-1} &= \mathbf{U}_{n+1} + \frac{\partial \mathbf{U}_{n+1}}{\partial t}(t_{n-1} - t_{n+1}) + \frac{\partial^2 \mathbf{U}_{n+1}}{\partial t^2}\frac{(t_{n-1} - t_{n+1})^2}{2} + \mathcal{O}\left((t_{n-1} - t_{n+1})^3\right)
\end{aligned}$$

These expressions can be used to obtain difference formulas that allow for time stepping that is first-order ($p = 1$) or second-order ($p = 2$) accurate in time. The coefficients for these schemes are

$\mathbf{p}$	$\alpha_{\mathbf{t}}$	$\beta_{\mathbf{t}}$	$\gamma_{\mathbf{t}}$
1	$\frac{1}{\Delta t_{n+1}}$	$\frac{-1}{\Delta t_{n+1}}$	0
2	$-\beta_t - \gamma_t$	$-\left[\frac{1}{\Delta t_{n+1}} + \frac{1}{\Delta t_n}\right]$	$\frac{\Delta t_{n+1}}{\Delta t_n \left(\Delta t_{n+1} + \Delta t_n\right)}$

Table 3.1: Coefficients for time discretization schemes

presented in Table 3.1.

$$\frac{\partial \mathbf{U}_{n+1}}{\partial t} = \alpha_t \mathbf{U}_{n+1} + \beta_t \mathbf{U}_n + \gamma_t \mathbf{U}_{n-1} + \mathcal{O}\left(\Delta t_{n+1}^p\right) \tag{3.20}$$

The system of equations defined by 3.17 can be written in residual form to form a non-linear algebraic system as a function of the unknown nodal values $\mathbf{U}_{n+1} \equiv \mathbf{U}_h\left(t_{n+1}\right)$:

$$\mathbf{R}\left(\mathbf{U}_{n+1}\right) = 0 \tag{3.21}$$

Equation 3.21 can be reduced to a series of linear problems, which upon solving, converge to the solution, $\mathbf{U}_{n+1}$, of the non-linear system. Taylor series expansion of Equation 3.21 about iterate $\mathbf{U}_{n+1}^l$ can be used to derive the expression for Newton's method:

$$\left[\frac{\partial \mathbf{R}\left(\mathbf{U}_{n+1}^l\right)}{\partial \mathbf{U}_{n+1}}\right] \delta \mathbf{U}_{n+1}^{l+1} = -\mathbf{R}\left(\mathbf{U}_{n+1}^l\right) \tag{3.22}$$

where $\frac{\partial \mathbf{R}}{\partial \mathbf{U}}$ is the Jacobian for the non-linear system and $\delta \mathbf{U}_{n+1}^{l+1} = \mathbf{U}_{n+1}^{l+1} - \mathbf{U}_{n+1}^l$. Thus, an implicit linear system for $\delta \mathbf{U}_{n+1}^{l+1}$ is obtained which when solved for a sequence of iterates ($l = 0, 1, ...$) converges to $\mathbf{U}_{n+1}$. The Newton method provides second-order conditional convergence where residuals decrease quadratically if the intial guess is close enough to the final solution. Both $\frac{\partial \mathbf{R}}{\partial \mathbf{U}}$ and $\mathbf{R}\left(\mathbf{U}_{n+1}^l\right)$ are stored while solving Equation 3.22. Since the system matrix is large but sparse (due to the use of piecewise-linear elements), storing it efficiently is critical. FIN-S makes use of the parallel sparse matrix format available through the PETSc toolkit, along with PETSc iterative solvers [47].

The system matrix once computed, can also be modified for use as a preconditioner. A parallel block-Jacobi ILU-0 preconditioner has been used for the present work [48, 49]. The matrix-vector product can be obtained directly after calculating the system matrix and the preconditioner.

Steady state simulations undertaken during the course of the current study have been carried out using a first-order accurate time discretization, with only one iteration of the approximate newton solve per time-step. Time accurate studies on the other hand have been run using a second-order time accurate scheme with multiple Newton sub-iterations (3-5) per time step.

3.5 Electric Field Coupling

The flow-field in the arc-jet has been computed by loosely coupling the electric field with the flow solver. Although, this coupling strategy can have an adverse impact on the convergence properties of the overall simulation, it minimizes computational costs at each time step and provides for ease of implementation. The computed flow solution for a given time-step, is used for calculating the electric field. This is achieved by extracting the state of the gaseous mixture at every node point in order to calculate the electrical conductivity, σ, using Equation 2.49. This distribution for σ is then plugged into the electric field equation (2.10) to solve for ϕ, and obtain electric current and the Joule heating term. The contribution of the Joule heating is treated as an explicit source term and is held constant while integrating the system of flow equations for the next time step. The Joule heating adds energy to the flow-field, which modifies the state of the system. This in turn changes the electrical conductivity, and results in an altered electrical field distribution. Therefore, a two-way coupling is established between the flow solution and the associated electric field. Similar solution procedures have been used for linking hypersonic reacting flows with radiative heat transfer and surface ablation models [50].

The weak form of the electric field equation (2.10) can be obtained by multiplying by an appropriate set of test functions $\mathbf{W}$ and then integrating over the entire domain Ω. Equation 2.10 being elliptic in nature, is ideal for solving through the standard Galerkin formulation and requires no biasing through additional stabilization terms. The approximate finite element discretization

of the weak form of the electric field equation, using the test functions, $\mathbf{W}_h$, and the approximate solution, ϕ_h, is as follows:

$$\sum_{e=1}^{n_{el}} \int_{\Omega_e} \sigma_h \frac{\partial \mathbf{W}_h}{\partial x_i} \cdot \frac{\partial \phi_h}{\partial x_i} \, d\Omega - \sum_{e=1}^{n_{el}} \int_{\Gamma_e} \mathbf{W} \, \epsilon_h \, d\Gamma \; = \; 0 \tag{3.23}$$

The last term in Equation 3.23 is the normal component of the imposed current density, $\epsilon_h \; = \; \overrightarrow{\mathcal{J}} \, . \, \hat{n}$, where $\overrightarrow{\mathcal{J}} \; = \; \overrightarrow{J}_{imposed}$ at a given node point on the prescribed boundary surface. $\phi_h \left(\mathbf{x}, t \right)$ and $\sigma_h \left(\mathbf{x}, t \right)$ can be reconstructed through a linear combination of the nodal solution values, $\phi_h \left(\mathbf{x}_j, t \right)$, and $\sigma_h \left(\mathbf{x}_j, t \right)$ with the finite element basis functions $(\mathcal{N}_j)$ as the coefficients.

$$\phi_h \left(\mathbf{x}, t \right) \;\; = \;\; \sum_j \mathcal{N}_j(\mathbf{x}) \, \phi_h \left(\mathbf{x}_j, t \right) \tag{3.24}$$

$$\sigma_h \left(\mathbf{x}, t \right) \;\; = \;\; \sum_j \mathcal{N}_j(\mathbf{x}) \, \sigma_h \left(\mathbf{x}_j, t \right) \tag{3.25}$$

Boundary Conditions

$\phi = 0$ is imposed at the cathode. Since, the arc is powered by a constant-current source, a constant current density $\overrightarrow{\mathcal{J}} \; = \; \overrightarrow{J}_{imposed}$ calculated from the total current, I, is imposed at the anode.

$$\textbf{Cathode:} \qquad \phi \qquad\qquad = 0 \tag{3.26}$$

$$\begin{aligned} \textbf{Anode:} \qquad \int_{\Gamma_{anode}} \sigma \nabla \phi \, . \, \hat{n} \, d\Gamma \;\; &= \; - \int_{\Gamma_{anode}} \overrightarrow{J}_{imposed} \, . \hat{n} \, d\Gamma \\ &= \; I \end{aligned} \tag{3.27}$$

Additionally, in order to ensure current continuity at the cathode and allow the electrical current to enter the electrode from the flowstream, the electrical conductivity is defined as $\sigma \; = \; max \left(\sigma_{calc}, \, 8.10^3 \right)$ (σ and σ_{calc} are in $S\text{-}m^{-1}$, where σ_{calc} is the electrical conductivity computed using the state of the plasma at a given point). Although, this results in an unphysically high current density at the electrode surface, it provides for a stable arc attachment with no impact on the accuracy of the overall solution in the flow chamber.

Chapter 4

Results

This chapter presents results obtained for both atmospheric entry flights and ground based arc-jet testing. The capabilities of the developed multi-physics simulation framework are demonstrated by modeling the vastly different flow regimes and associated physical phenomena encountered in these two problems. Consequently, the focus is not only on presenting solutions but also on describing the methodology for these challenging simulations.

4.1 Hypersonic Atmospheric Entry

The combination of FIN-S and the updated version of Mutation++ provides the perfect platform for modeling flows found in the vicinity of high speed atmospheric entry vehicles, which are characterized by thermal and chemical non-equilibrium and the presence of strong shocks waves. The free-stream conditions encountered during the Flight Investigation of Re-entry Environment (FIRE) experiment have been used to obtain solutions for hypersonic flow around an axisymmetric bluff body [51, 52]. Project FIRE was an attempt at investigating re-entry heating rates on a sub-scale Apollo configuration at lunar-return entry velocity. The experimental aero-thermal data from the FIRE project has been extensively used for designing re-entry systems and for validating a multitude of CFD codes. Employing free-stream conditions observed at different points along the FIRE II trajectory opens up a rich body of work for code-to-code comparison [53] and validation using experimental data. The first case presented in this section simulates re-entry conditions at 1643 s for the FIRE II experiment. The second case employs the same conditions but with the free-stream velocity increased considerably, resulting in a numerically stiffer problem.

4.1.1 CASE 1: FIRE II

Problem Description and Solution Procedure

The 1643 s case entails an axisymmetric hypersonic viscous reacting laminar flow around a sphere of radius, $R_{wall} = 80.5$ cm. The free-stream variables have been defined using the following values:

$$\begin{aligned} u_\infty &= 10480 \text{ m/s} \\ \rho_\infty &= 7.80\times10^{-4} \text{ kg/m}^3 \\ T_\infty &= 276 \text{ K} \end{aligned}$$

The surface of the sphere is assumed to be a non-catalytic wall with $T_{wall} = 640$ K. The strong thermal non-equilibrium nature of the flow at the shock and after necessitates the use of a 2-Temperature model. Chemical kinetics, and thermodynamic and transport properties for the gas mixture are calculated using the Mutation++ library. The reaction mixture used in this study is Air-11 [54], with the elemental ratio fixed at N : O = 0.79 : 0.21.

The computational grid used for this case is presented in Figure 4.1. It consists of 60×100 elements in the circumferential and normal directions respectively. Care has been taken to ensure that the mesh edges in the circumferential direction align with the strong bow shock produced by the bluff body. Additionally, the mesh has been sufficiently refined in the normal direction to resolve the boundary layer near the surface and to ensure that the jump across the shock occurs over multiple grid points. A uniform initial solution based on the free-stream values is used. Time-marching is used until the normalized unsteady flow residual decreases by 6 orders of magnitude.

$$(\mathcal{R}_n)_{normal} = \frac{\mathcal{R}_n}{\mathcal{R}_1} = \left\| \frac{\Delta \mathbf{U}_{n+1}}{\Delta t} \right\|_\infty \leq 10^{-6} \tag{4.1}$$

The inflow boundary uses supersonic inlet boundary conditions (BC) and the downstream outflow BC is defined as supersonic outflow. A no-slip convective wall boundary with $h_w = 1000$ is used initially to accelerate the process of the shock moving upstream from the wall surface towards

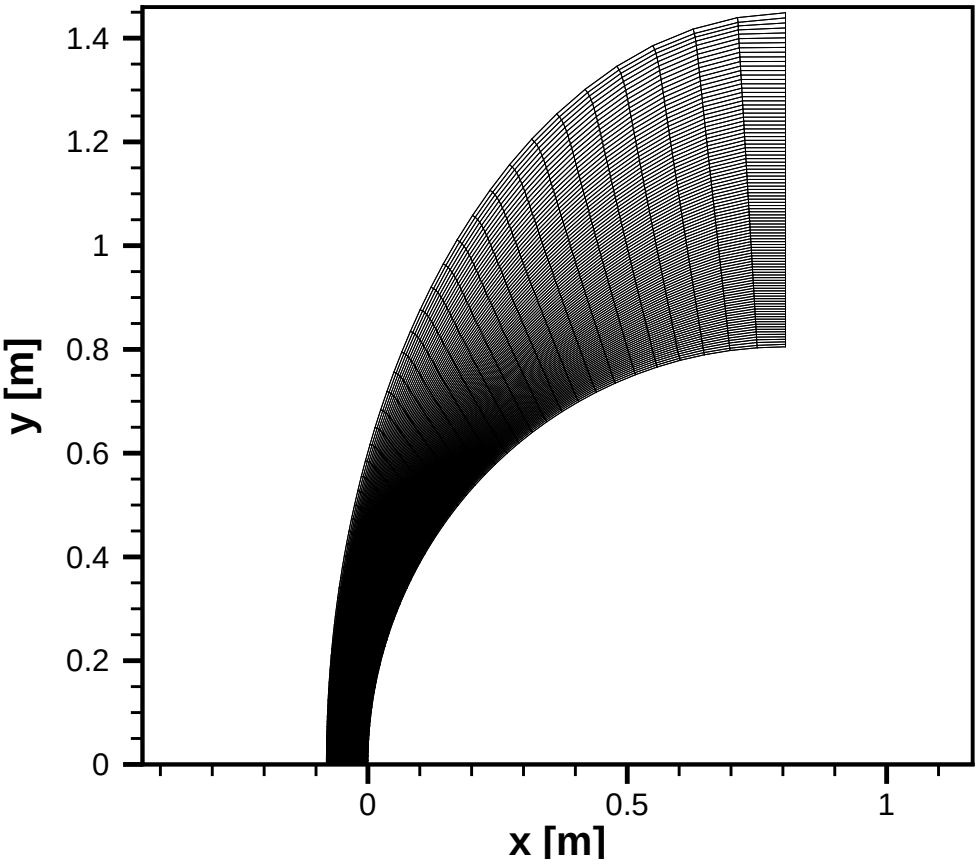

Figure 4.1: Computational grid for FIRE II 1643 s case

its final steady state location. Once the shock layer has traversed far enough from the wall, the simulation is restarted with an isothermal boundary condition at the wall.

Flow-field and Stagnation Line Properties

The steady flow-field for Case 1 is shown in Figure 4.2. A strong bow shock with a discontinuous change in properties develops upstream to the body. A subsonic high temperature region behind the shock in the proximity of the body axis is also formed, along with an expansion zone where the flow cools down and accelerates. There is an increase in total pressure, density, and temperature

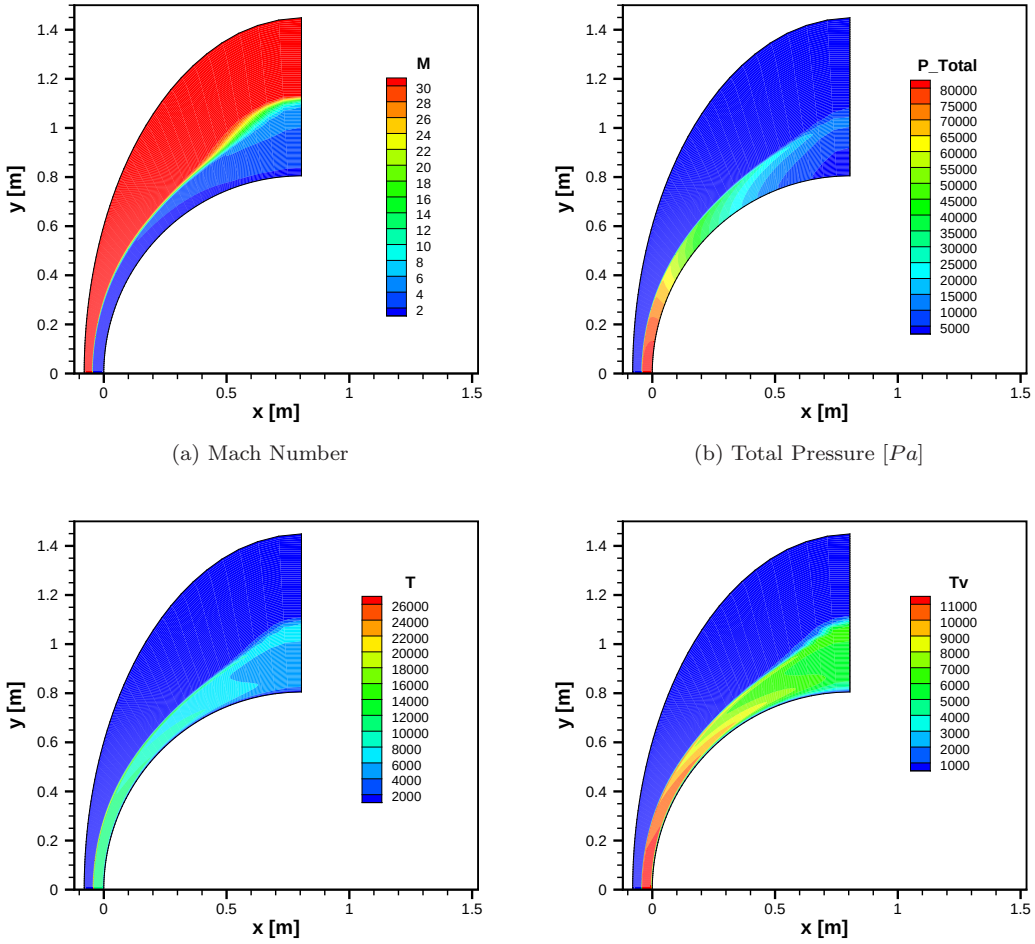

(a) Mach Number

(b) Total Pressure $[Pa]$

(c) Translational-rotational temperature $[K]$

(d) Electronic-vibrational temperature $[K]$

Figure 4.2: Steady state flowfield for FIRE II 1643 s case

and a corresponding decrease in Mach number across the shock. An interesting feature of the flow-field is the temperature distribution, which is starkly different from solutions obtained for a typical calorically perfect gas in which the post-shock stagnation region temperature remains largely constant. The shock thickness appears more diffused in the downstream region, away from the forebody centerline. This can be attributed to the slight misalignment between the mesh edges and the shock in that region.

A knowledge of the chemical composition and distribution of internal energy modes is critical for characterizing weak plasmas that are generated in the post shock region. Figures 4.3 presents the evolution of translational-rotational (T) and electronic-vibrational (T_v) temperatures along the stagnation line. The shock stand-off distance predicted using the current framework shows excellent agreement with results obtained by Hash et al. using the DPLR baseline code [53]. Differences in the exact distribution of flow properties stem from the use of different computational meshes, physical models and reaction and property databases.The jump in T across the shock is followed by a re-distribution of energy among the internal modes and the onset of chemical reactions. This ultimately results in a post-shock equilibrium state. The electronic-vibrational temperature initially increases rapidly but levels off due to the activation of chemical reactions.

The degree of thermal non-equilibrium is strongly contingent on the nature of the coupling between internal energy and chemistry. Figures 4.4 and 4.5 show the degree of ionization and species distribution along the stagnation line. The use of a geometric average temperature as the rate controlling temperature retards dissociation. Thus, the sharp jump in T and the corresponding low value for T_v is not only indicative of thermal non-equilibrium but also points towards delayed dissociation and chemical non-equilibrium. The largest contribution to the formation of free electrons appears to be coming from atomic nitrogen with significant contribution from atomic oxygen as well. Ionized molecular oxygen, nitrogen and NO appeared to be formed immediately after the shock, but their mole fractions decrease rapidly as molecules dissociate and the flow reaches equilibrium. A strong consideration while estimating the extent of thermal non-equilibrium for these classes of flows is the dissipation rate of free-electron energy by the excitation and ionization of atomic species. The kinetic energy lost by free-electrons during electron-impact ionization has

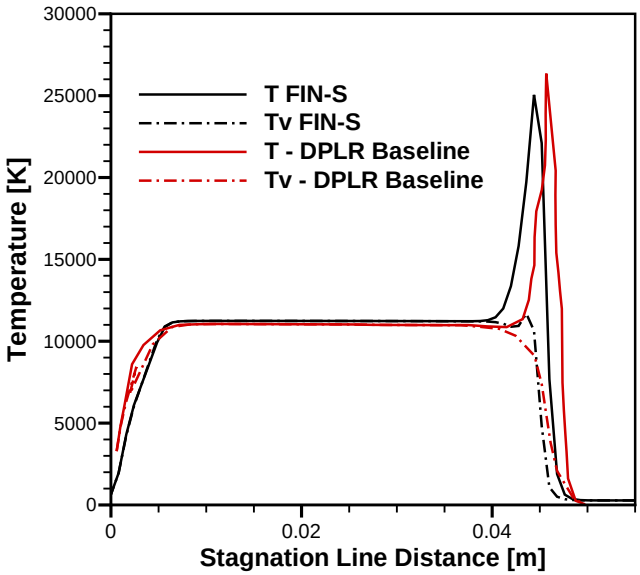

Figure 4.3: Temperature distribution along stagnation line for FIRE II 1643 s case

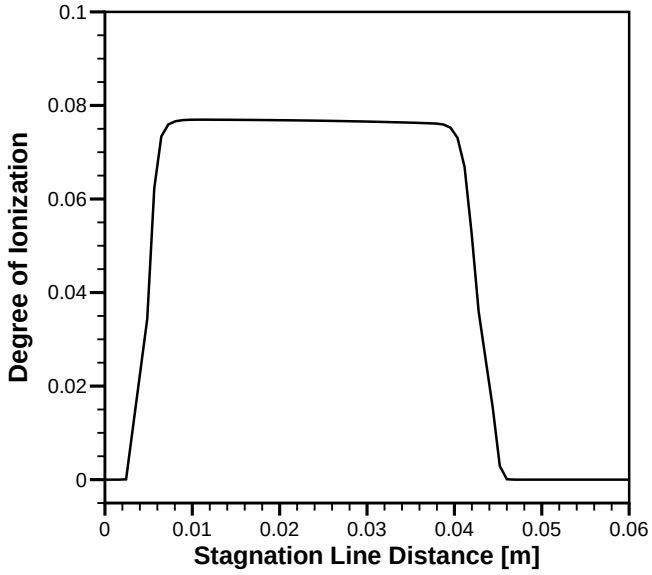

Figure 4.4: Degree of ionization along stagnation line for FIRE II 1643 s case

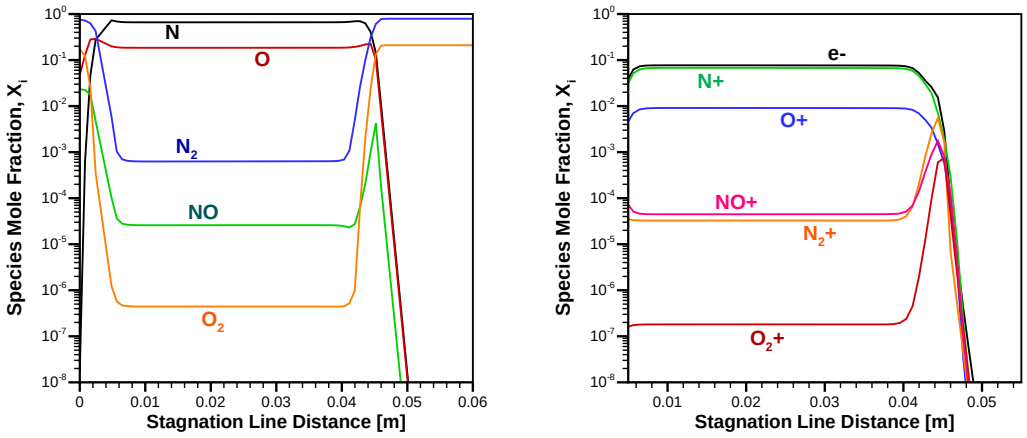

(a) Neutral species

(b) Ionized species

Figure 4.5: Species mole-fractions along stagnation line for FIRE II 1643 s case

a tendency to slow down further reactions, decelerating the process of thermal equilibration, *i.e.* conversion of translational energy into internal energy. A major component of this loss comes from exciting the electronic states of the constituent species, which makes the role of radiation and the need to accurately model it absolutely crucial for predicting the dynamics of thermal and chemical relaxation.

4.1.2 CASE 2: $u_\infty = 16\ km/s$

Problem Description and Solution Procedure

The set of conditions used for Case 2 are the same as Case 1, with the only difference being an increase in the freestream velocity to simulate a Mars sample return case. Therefore, the free-stream variables used to define the problem are:

$$\begin{aligned} u_\infty &= 16000 \text{ m/s} \\ \rho_\infty &= 7.80\times10^{-4} \text{ kg/m}^3 \\ T_\infty &= 276 \text{ K} \end{aligned}$$

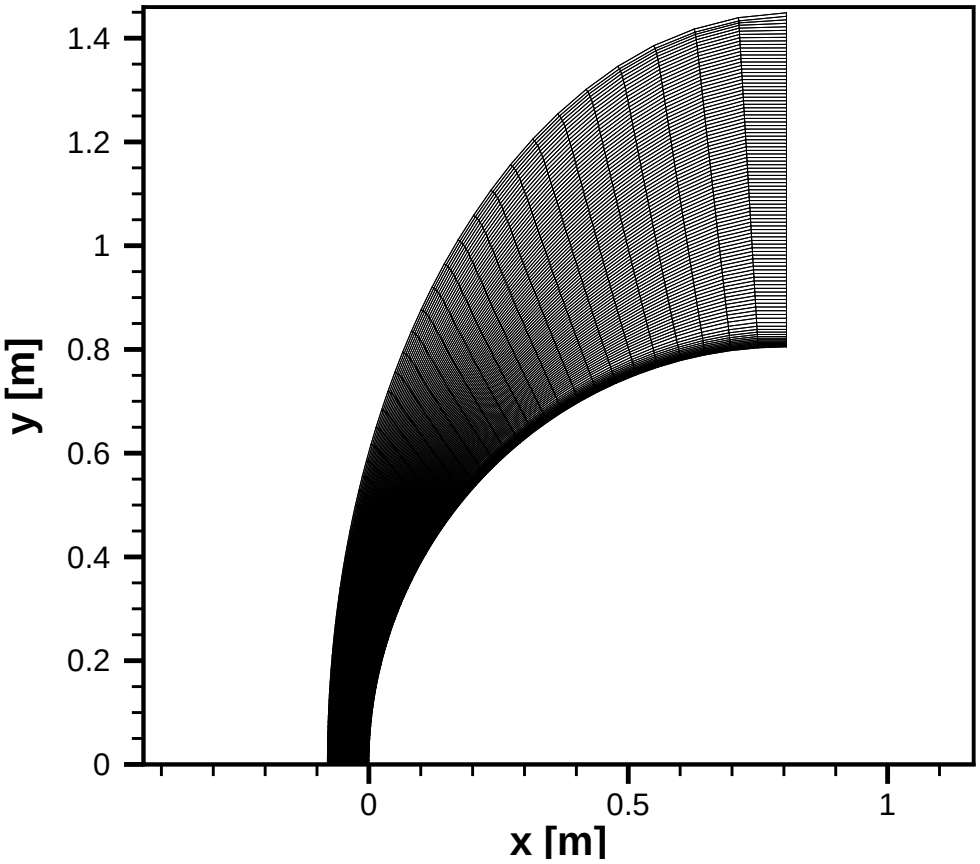

Figure 4.6: Computational grid for Case 2: $u_\infty = 16\ km/s$

The geometry employed is identical to Case 1. The surface of the bluff body is assumed to be non-catalytic and $T_{wall} = 640$ K. The flow-field has been simulated using a 2-Temperature model and Air-11 as the reaction mixture. The computational grid used for Case 2 (Figure 4.6) consists of the same number of elements (60×100), with only minor modifications made in the mesh alignment to accommodate changes in the shock location and curvature. Similar considerations with regards to resolving the boundary layer and the bow shock have been made while refining the mesh. A uniform initial solution based on the free-stream conditions is used. Time-marching for convergence upto 6 orders of magnitude has been carried out. Supersonic inflow and outflow boundary conditions have

been prescribed on the domain inlet and outlet. A solution strategy employing both convective and isothermal type wall boundary conditions has been employed to accelerate convergence.

Flow-field and Stagnation Line Properties

The steady state flow-field for Case 2 is presented in Figure 4.7. As expected, a stronger discontinuity across the shock occurs and therefore, the spike in total pressure, temperatures, and density is larger for Case 2. The shock layer again appears to be slightly under-resolved in the downstream region, which is due to mesh edges cutting across the shock face.

Figure 4.8a illustrates the variation in T and T_v along the stagnation line. The bow shock is formed closer to the body and the temperatures immediately in the post shock region and further downstream are obviously higher. In contrast to results obtained for Case 1, there appears to be no overshoot in the electronic-vibrational temperature after the shock. Figures 4.8b and 4.9 show the degree of ionization and the distribution of species mole-fractions along the stagnation line. A key feature of the obtained flow solution is the faster rate of thermal and chemical equilibration which results in the equilibrium state being attained closer downstream to the shock as compared to Case 1. This is a direct consequence of the higher total pressure and density encountered behind the shock, which results in an increased rate of collisions between particles, accelerating chemical reactions and the re-distribution of energy in the internal modes. The reaction mixture is ionized to a greater extent and the post-shock equilibrium electron mole fraction is close to 0.38. Atomic nitrogen again appears to be the largest source of free-electrons, followed by atomic oxygen. The reaction mixture contains ionized molecular oxygen, nitrogen and NO in the immediate vicinity of the shock but they dissociate as the flow moves downstream.

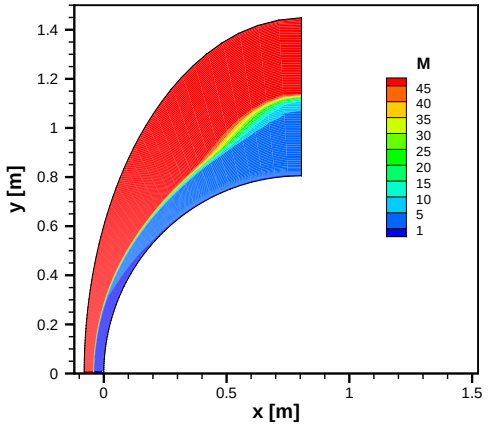

(a) Mach Number

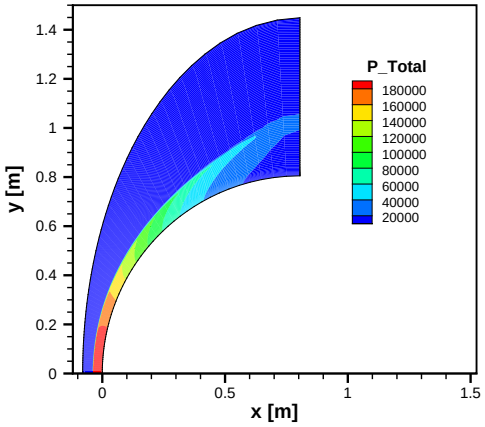

(b) Total Pressure $[Pa]$

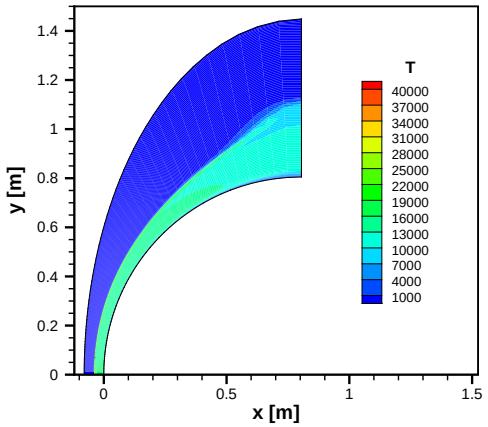

(c) Translational-rotational temperature $[K]$

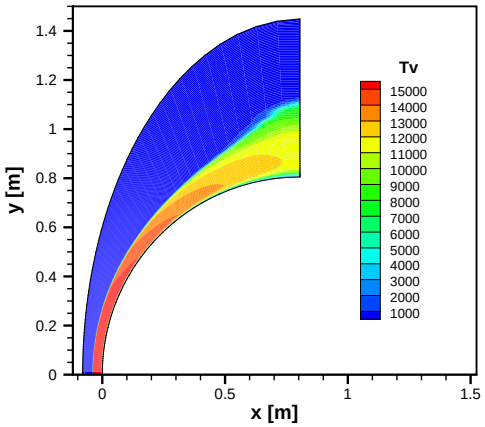

(d) Electronic-vibrational temperature $[K]$

Figure 4.7: Steady state flowfield for Case 2: $u_\infty = 16\ km/s$

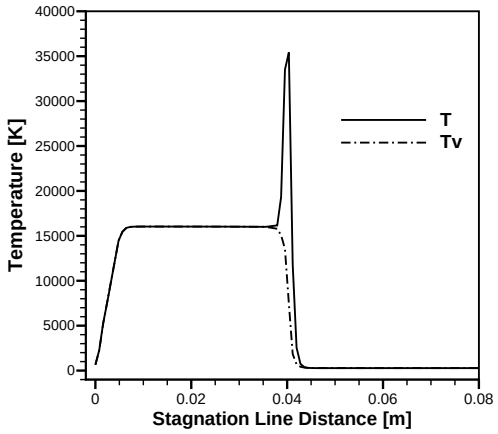

(a) Temperature distribution

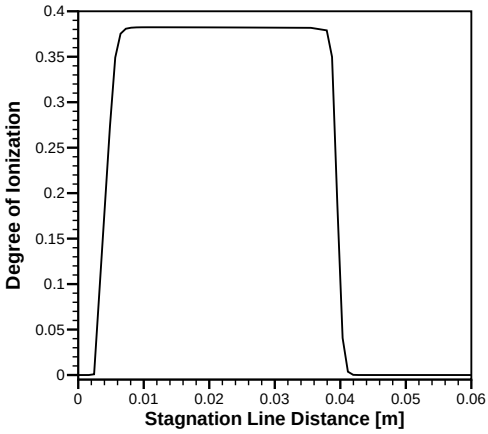

(b) Degree of ionization

Figure 4.8: Temperatures and degree of ionization along stagnation line for Case 2: $u_\infty = 16\ km/s$

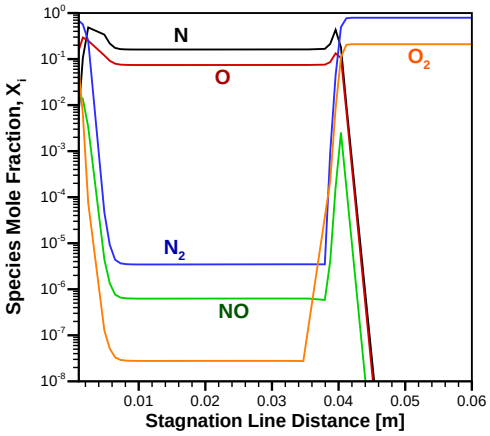

(a) Neutral species

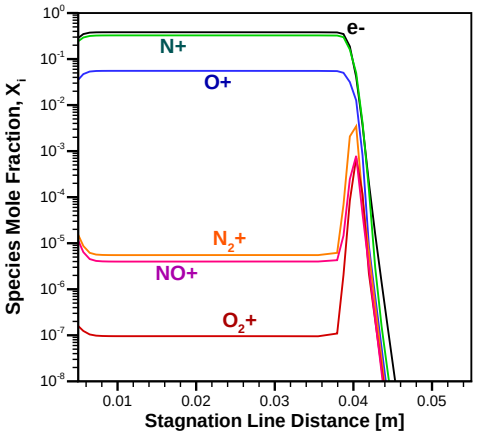

(b) Ionized species

Figure 4.9: Species mole-fractions along stagnation line for Case 2: $u_\infty = 16\ km/s$

4.2 Aerodynamic Heating Facility

4.2.1 Problem Description and Solution Procedure

There have been multiple studies that have attempted to model the distribution of flow variables such as temperature, enthalpy, and species composition in an arc-jet [55, 56]. The AHF and the Ames 60 MW Interaction Heating Facility (IHF) have recently been investigated using three codes named ARCFLO2, ARCFLO3, and ARCFLO4 [57, 58, 59, 60, 61], which assume the flow to be axis-symmetric and incorporate a heating section with a turbulence and radiation model. Takahashi et al. [62] have studied various arc heaters such as the constrictor-type (Kyushu University Wind Tunnel) and segmented-type arc heaters (JAXA Wind Tunnel and AHF) using multi-temperature Reynolds-averaged Navier-Stokes equations with a three-band radiation model developed by Sakai and Olejniczak [59, 61].

The high enthalpy reacting flows and the associated electric field in the AHF have been simulated in the present work with the following assumptions: 1) The flow is considered to be turbulent, steady, continuum and axisymmetric. 2) The injected test gas mixture is Argon-3, which reduces computational costs and provides first order estimates for operating conditions. 3) A single temperature, T, is used for defining the total internal energy of the flow. 4) The flow-field is in a state of chemical non-equilibrium. 5) The arc current is not large enough to induce an effective magnetic field. Consequently, Lorentz force, Hall current, and ion slip are neglected. 6) The effects of radiation are not considered.

The internal geometry of the constricted arc heater and the nozzle assembly that constitute the 20 MW AHF at NASA Ames is presented in Figure 4.10. The test gas is injected through the segmented disks along the length of the constrictor. The flow in the facility has an azimuthal (swirl) velocity component designed to enhance mixing and to stabilize the arc current. A small amount of argon is also introduced in the anode chamber to shield the electrodes. The walls of the heater are water cooled to counteract the effect of the large amount of heating due to electrical discharge.

The computational grid that we use for modeling this complex facility introduces certain sim-

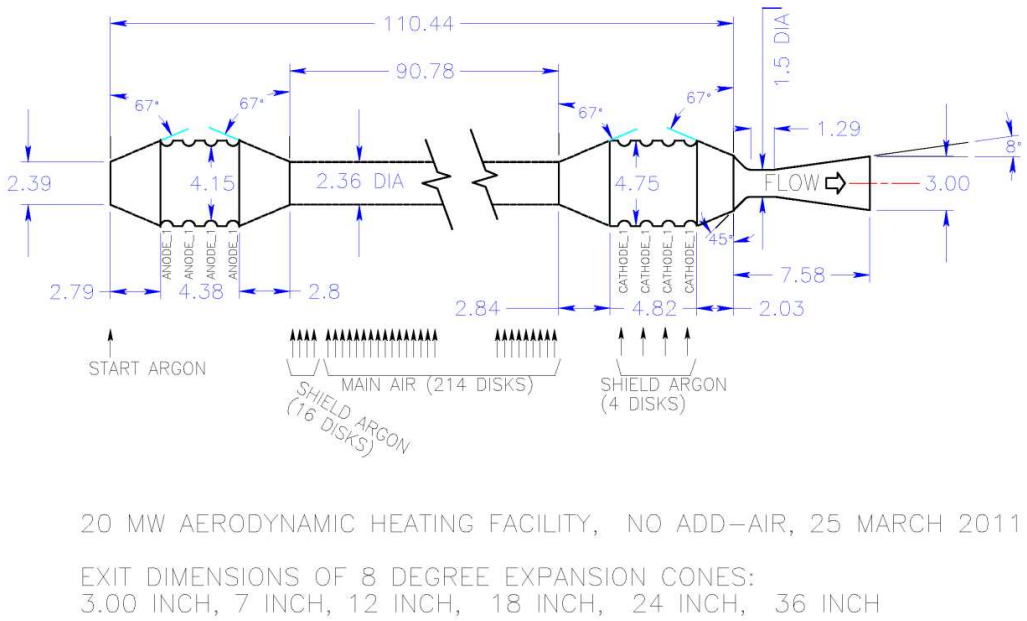

Figure 4.10: Internal geometry of the 20 MW Aerodynamic Heating Facility (AHF) (Source: NASA Ames Research Center)

Section	**Start coordinate [m]**	**End coordinate [m]**
Anode	-2.82	-2.56
Constrictor	-2.56	-0.27
Cathode	-0.27	0.00
Throat	0.00	0.03
Nozzle	0.03	0.18

Table 4.1: Demarcation between different AHF sections along the axial direction

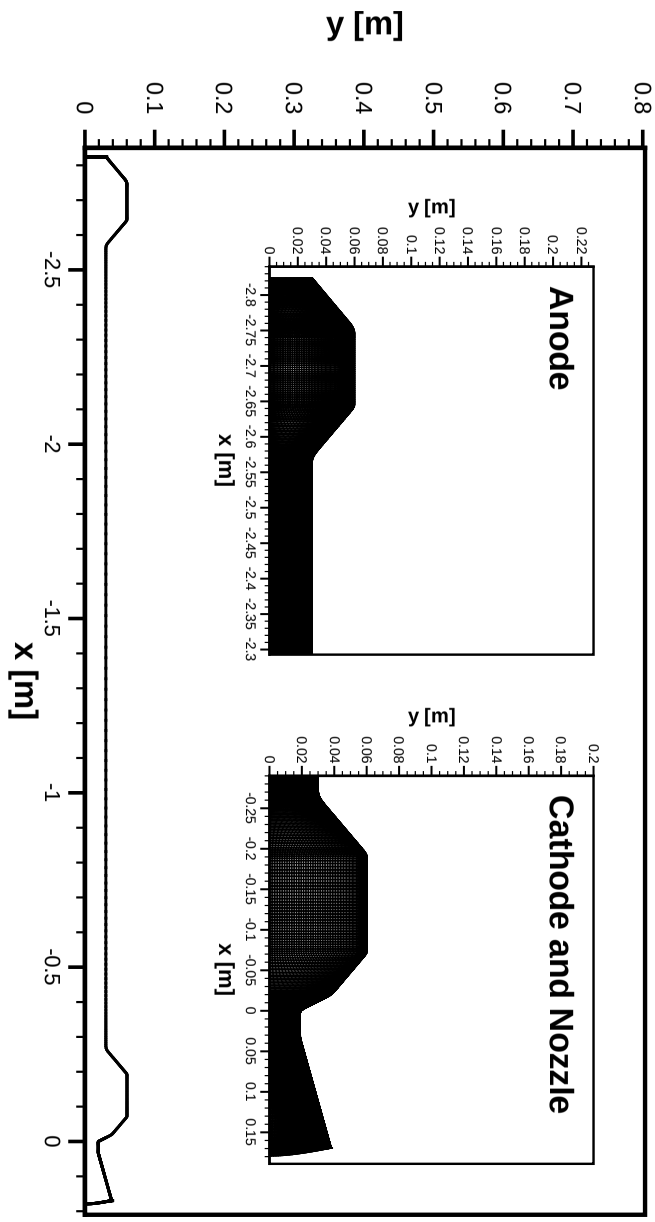

Figure 4.11: Computational grid for modeling the 20 MW Aerodynamic Heating Facility (AHF)

Wall temperature, K	1000
Total current, A	1600
Constrictor mass injection rate, g/s	0.5
Anode mass injection rate, g/s	0.25

Table 4.2: AHF operating parameters

plifications to the geometry. It is composed of 85×425 elements in the radial and axial directions respectively. The origin for the computational domain is located on the centerline at the beginning of the throat. The different sections that constitute the facility have been demarcated in the axial direction according to Table 4.1. The grooves created by the series of discrete electrode packages comprising of alternating copper rings and spacer disks have been replaced by a continuous straight edge of equivalent length which acts as the electrode surface. The electrically conducting edge is positioned in the middle of the horizontal wall section in both the anode and cathode chamber. This ensures that each electrode is surrounded by a strip of insulation that prevents the current from flowing too close to the walls. Chamfering has been carried out at all corner points. These changes represent only a minor deviation from the original layout and are expected to have a minimal impact on the final solutions.

The operating parameters for the AHF are listed in Table 4.2. The flow-field in the AHF is initialized using the following values:

$$
\begin{aligned}
u_{initial} &= 10^{-3} \text{ m/s} \\
\rho_{initial} &= 5.84 \text{ kg/m}^3 \\
T_{initial} &= 1000 \text{ K} \\
P_{initial} &= 12 \text{ atm}
\end{aligned}
$$

An isothermal no-slip boundary condition is prescribed on the walls for the converging-diverging (C/D) nozzle. A convection type boundary condition, with $h_w = 10^5$ is imposed on all other walls, where the specified wall temperature is simply analogous to the target temperature. This results

in improved convergence and reduces stiffness, especially in the presence of strong temperature gradients created due to the electrical discharge. A test gas mixture consisting of Argon-3 at equilibrium composition is injected from the electrically conductive edge section in the anode and the walls of the constrictor using a mass injection wall boundary condition. Constant current density computed from the total current value is imposed on the anode while the electric potential for the cathode is fixed at zero. ν_{SA} was assigned an initial value of $5\,\nu_{initial}$, where $\nu_{initial}$ is the kinematic viscosity of the initial flow-field. $\nu_{SA} = 0$ has been enforced at the walls. Since, the C/D nozzle exits into a test chamber at very low pressure, a vacuum exit type outflow condition is used. This entails reducing the specified exit pressure incrementally at each time step until the flow turns supersonic; the supersonic outflow boundary condtion is used subsequently.

The process of coupling the electric field with the flow solver initially results in a massive upsurge in instabilities in the flow domain. "Switching on" the electric field is akin to a detonation occurring in the narrowed confines of the constrictor which causes an instant rise in temperature and the flow being pushed outwards from both its ends. The flow-field eventually stabilizes with a well-defined path, comprising of hot gases, forming for the electric current. The debilitating effect of this transient period of chaos on the overall stability of the flow simulation is managed by gradually ramping up the total current, I_n, being imposed at the anode for a given time step:

$$I_n = I_{max} \frac{n}{c}$$

where I_{max} is the maximum total current listed in Table 4.2 and n is the current time step count. c is the current growth factor which needs to be adjusted for a given set of initial and operating conditions and has been fixed at 10^3. Time-marching has been carried for convergence upto 4 order of magnitude. The normalized unsteady residual increases initially with more current being introduced in the flow-field. The residual eventually starts decreasing but stagnates at a value of approximately 10^{-4}. Although, the flow features at this point become well established, small perturbations get introduced due to oscillating re-circulation regions, thereby, retarding further convergence.

4.2.2 Simulation Results

The physicochemical characteristics of the AHF can be better understood by analyzing the distribution of various properties in the entire flow domain and along the centerline. Figure 4.12 shows the flow streamlines in the AHF arc-heater and the adjoining nozzle assembly. The effect of mass injection is clearly highlighted through this figure, with streamlines emanating from the constrictor walls and the anode. Re-circulation regions are formed both in the anode and cathode chambers. The anode re-circulation bubble is dynamic in nature and its size and strength continues oscillating. This introduces perturbations in the flow-field, which owing to the loose coupling between the flow-solver and the electric field do not get dampened quickly enough. This has an adverse impact on the convergence properties of the simulation, resulting in the residual turning stagnant after a certain number of time steps have been completed, and the flow remaining unsteady.

Figure 4.13 presents the temperature distribution in the flow-field. The electrical discharge from the anode causes temperature in its immediate vicinity to increase sharply, resulting in strong gradients close to the electrode surface. The combination of mass injection and heat loss at the walls, causes a high temperature region to be formed along the centerline in the constrictor. The current density (Figure 4.14) mirrors the variation in temperature. A self-sustaining coupling is formed; higher temperature implies larger electrical conductivity, and results in greater electrical current flow and Joule heating. The gaseous mixture cools rapidly as it progresses through the throat and nozzle. The flow is completely subsonic in the heating section but accelerates to choke at the throat exit. The continuous expansion in the diverging section of the nozzle results in the flow going supersonic. The change in Mach number downstream to the cathode chamber has been illustrated in Figure 4.15.

Figure 4.16 presents the axial distribution of flow properties for the AHF. The observed temperature increases due to Joule heating, reaching its peak value in the constrictor. A sharp drop occurs due to the rapid expansion encountered in the nozzle. The high total pressure values observed in the heating section points towards enhanced particle collision rates. Thus, thermal equilibration occurs rapidly and a single temperature for characterizing the flow can be used. Takahashi et al. [62]

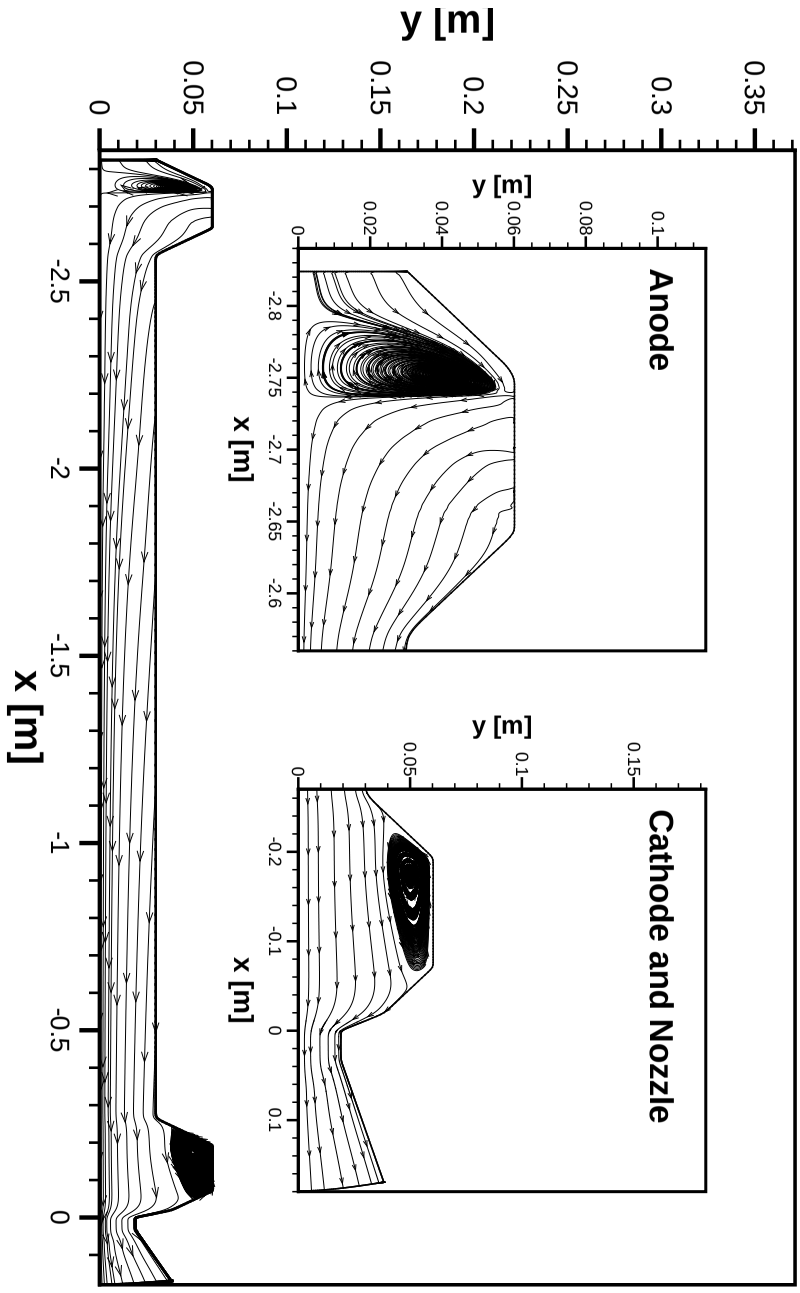

Figure 4.12: Flow streamlines in the 20 MW Aerodynamic Heating Facility (AHF)

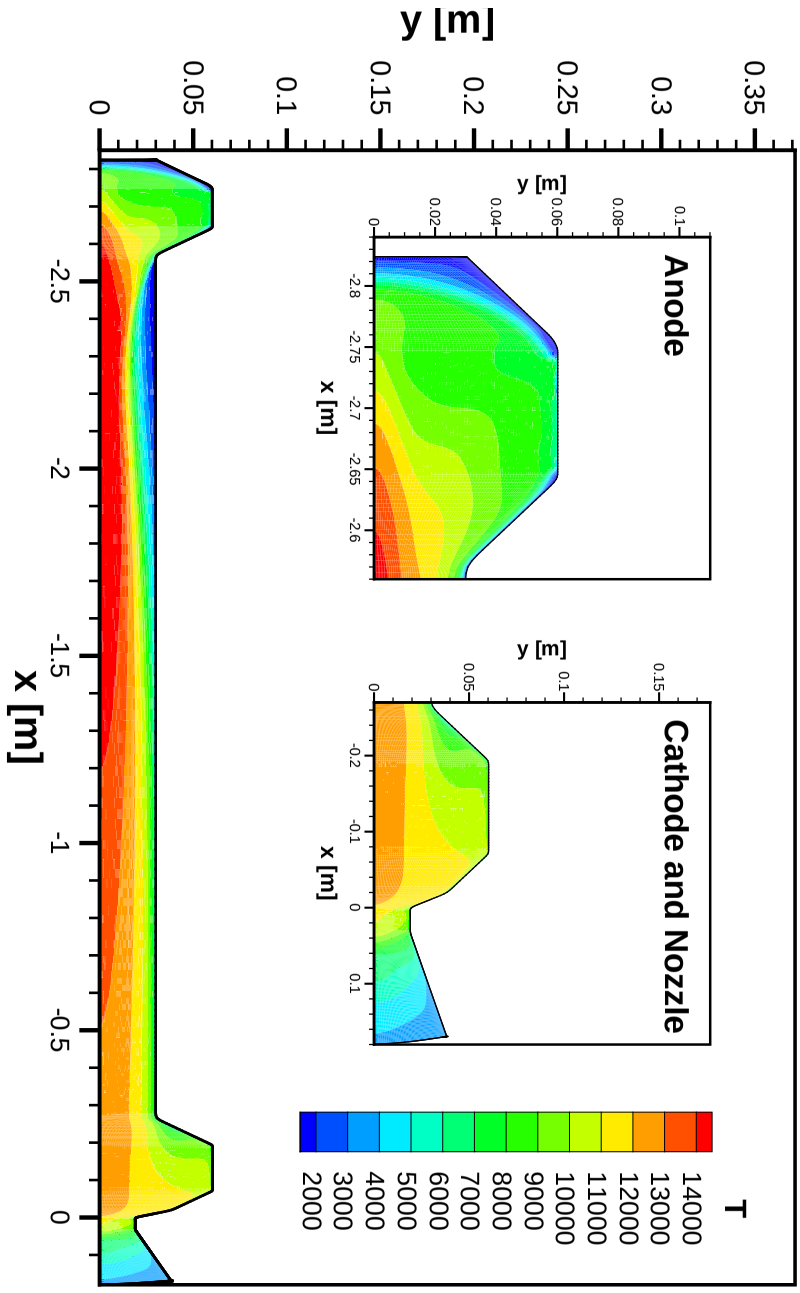

Figure 4.13: Temperature $[K]$ distribution in the 20 MW Aerodynamic Heating Facility (AHF)

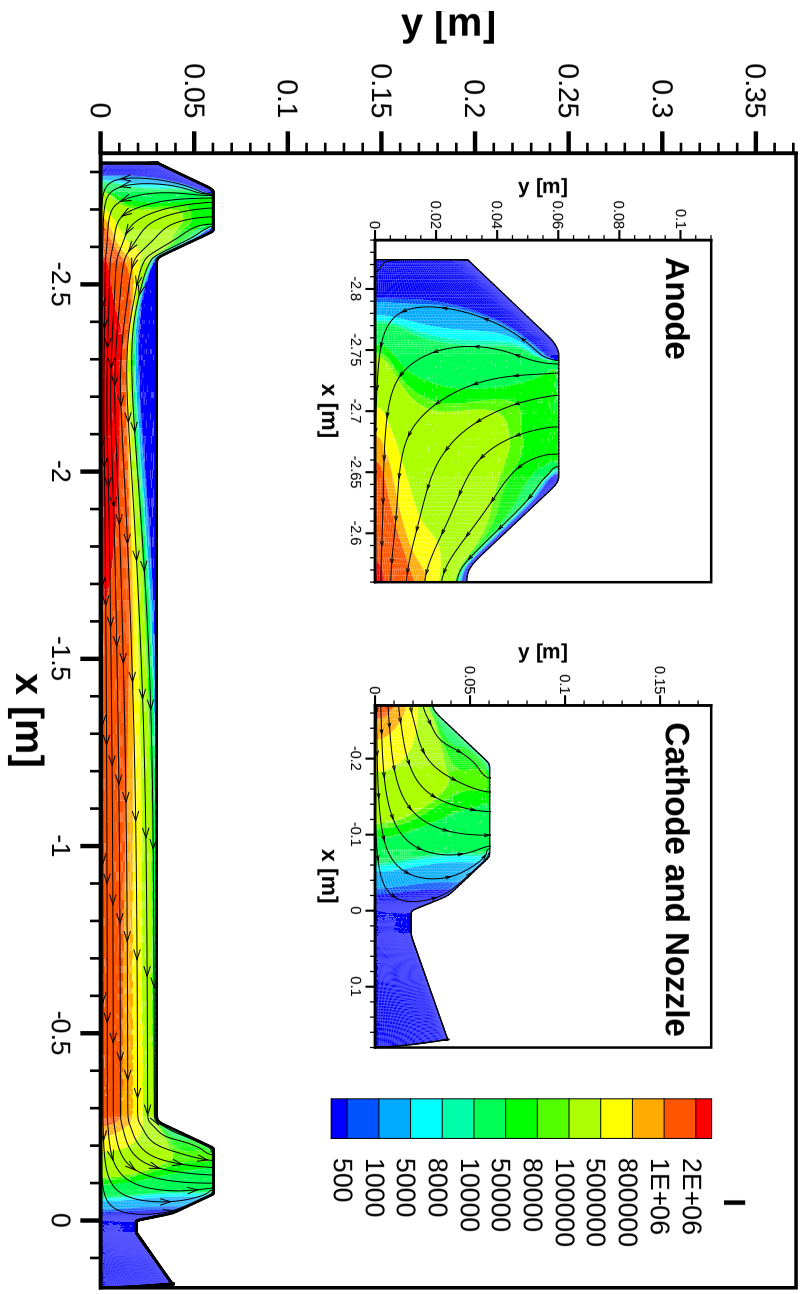

Figure 4.14: Current density $[A/m^2]$ distribution and current streamlines in the 20 MW Aerodynamic Heating Facility (AHF)

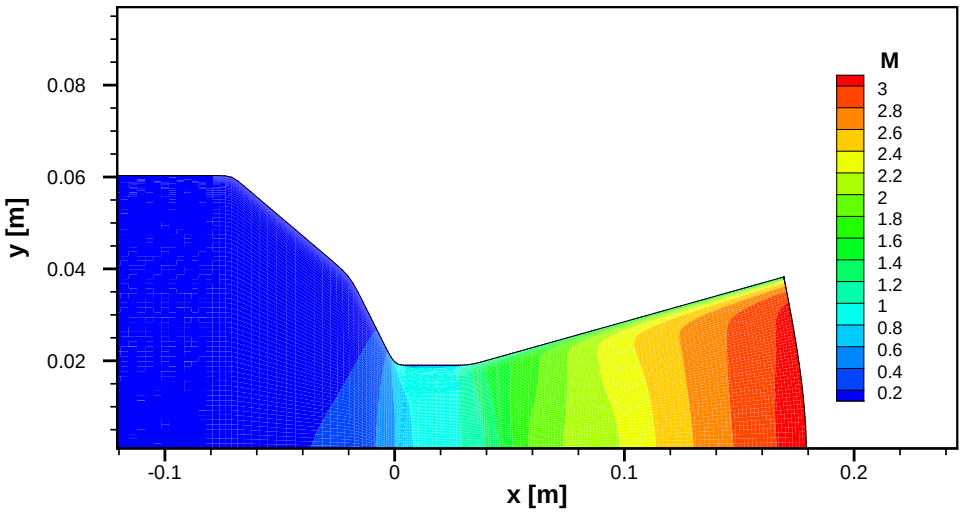

Figure 4.15: Mach number distribution in the 20 MW Aerodynamic Heating Facility (AHF)

have come to the same conclusion after studying the degree of thermal non-equilibrium by employing a 4-temperature model to model arc heaters. The expansion through the nozzle and the ensuing decrease in collision rate, coupled with a decline in the electron energy due to recombination reactions, introduces strong thermal non-equilibrium in the flow. Therefore, a more rigorous model for defining energies in each individual internal mode is required for modeling the flow in the converging-diverging nozzle assembly.

Ionization occurs in the arc column and results in the formation of free-electrons. These electrons are the primary current carriers for the electric discharge between the anode and cathode. Recombination reactions start to occur as the plasma approaches the nozzle. These reactions progress slowly and the energy released is not enough to arrest the decrease in temperature due to expansion. Flow properties remain largely constant along the axial direction in the constrictor. This feature can be exploited to compute the contribution of radiative flux by using the relatively inexpensive cylindrical slab method. Although the present work is focused on simulating the time-mean axisymetric current distribution observed in experiment facilities, the effect of unsteady near-wall current fluctuations needs to be further investigated to make better predictions.

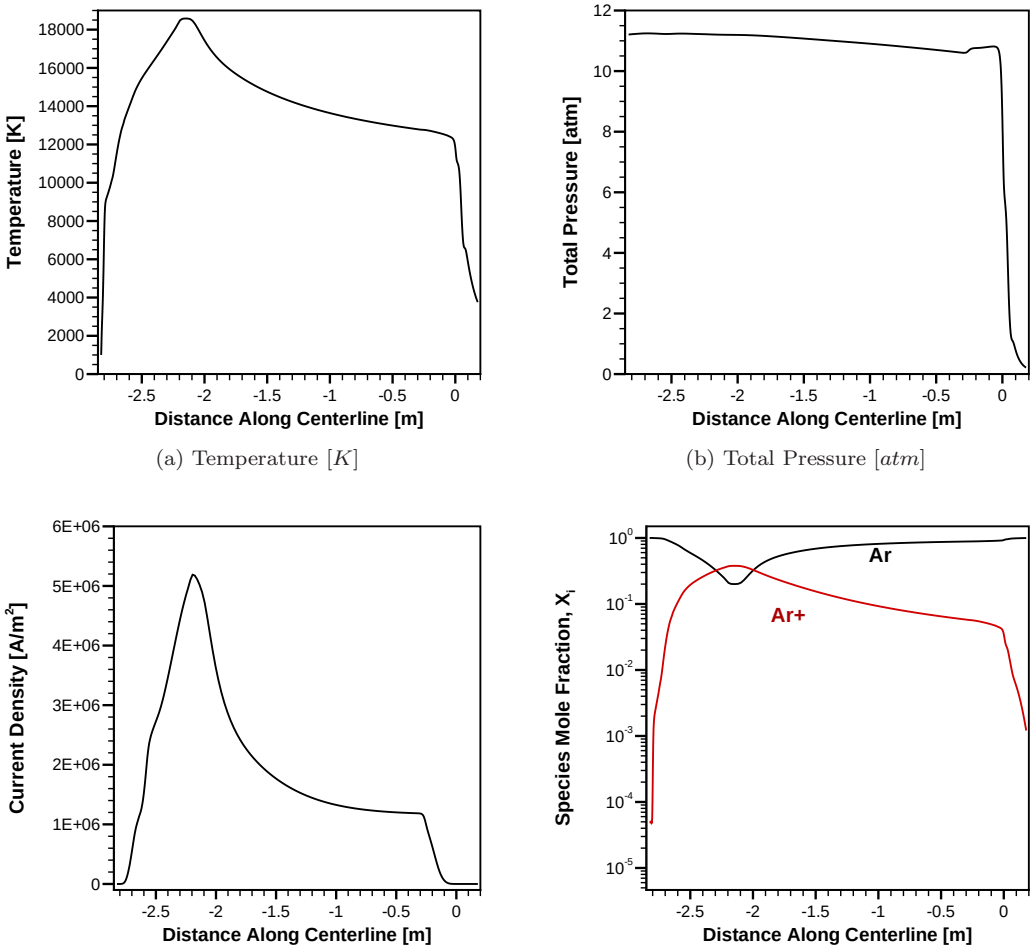

(a) Temperature $[K]$

(b) Total Pressure $[atm]$

(c) Current Density $[A/m^2]$

(d) Species Mole-fraction $[K]$

Figure 4.16: Flow properties along the centerline for the 20 MW Aerodynamic Heating Facility (AHF)

Chapter 5

Conclusions and Future Work

The most significant contribution of the current work has been the development of a new framework, built around enhancing the numerical capabilities of FIN-S with a new chemistry library, for accurate modeling of fluid flows in thermal and chemical non-equilibrium as well as adding the capability of imposing an electric field on the fluid. Robust routines that are based on efficient formulations for calculating thermodynamics and transport properties of the gas, and chemical and thermal relaxation in multi-temperature reaction mixtures have been added to the Mutation++ library. This implementation draws upon both the Chapman and Enskog method and simplified mixture rules to create a software toolkit that offers improved stability and sufficient accuracy for CFD analysis of high enthalpy flows. A separate module for simulating the effects of an applied electric field and adding the contribution of the Joule heating term to the energy equation, for quasi-neutral flows has been introduced through a two-way coupling with the flow solver. Thus, a whole spectrum of flow problems ranging from hypersonic vehicular re-entry to ground-based arc heated wind-tunnel testing can be studied using the same code. This versatility can have an immediate impact in devising test conditions for given flight conditions and interpreting experimental data to further refine the vehicle design process. Research work on improving the simulation framework is already underway and is directed towards investigating the following objectives:

1. Implementing a radiative tranport model, which is crucial for predicting the transfer of heat and momentum from the hot core to the cold wall region in large segmented-type constricted-arc heater facilities.

2. Performing a full three-dimensional analysis of the AHF in order to account for instabilities

in the azimuthal direction of swirling flows.

3. Modeling the full set of Maxwell equations to generate a more generalized description of the electro-magnetic interactions.

References

[1] DK Prabhu, David Saunders, Tomomi Oishi, Kristina Skokova, Jose Santos, Johnny Fu, Imelda Terrazas-Salinas, Enrique Carballo, and David Driver. Cfd analysis framework for arc-heated flowfields, i: Stagnation testing in arc-jets at nasa arc. *AIAA Paper*, 2081, 2009.

[2] AF Kolesnikov. Conditions of simulation of stagnation point heat transfer from a high-enthalpy flow. *Fluid dynamics*, 28(1):131–137, 1993.

[3] Benjamin S Kirk and Graham F Carey. Development and validation of a supg finite element scheme for the compressible Navier–Stokes equations using a modified inviscid flux discretization. *International journal for numerical methods in fluids*, 57(3):265–293, 2008.

[4] Benjamin S Kirk, Roy H Stogner, Todd A Oliver, and Paul T Bauman. Recent advancements in fully implicit numerical methods for hypersonic reacting flows. *AIAA Paper*, 2559, 2013.

[5] Benjamin S Kirk, John W Peterson, Roy H Stogner, and Graham F Carey. libmesh: a C++ library for parallel adaptive mesh refinement/coarsening simulations. *Engineering with Computers*, 22(3-4):237–254, 2006.

[6] Benjamin S Kirk. Fully-implicit Navier-Stokes (FIN-S). Technical report, NASA JSC-CN-20996, 2010.

[7] D Goodwin, N Malaya, H Moffat, and R Speth. Cantera: An object-oriented software toolkit for chemical kinetics, thermodynamics, and transport processes. Version 2.1 a1, 2012.

[8] Benjamin S Kirk, Steven W Bova, and Ryan B Bond. A streamline-upwind Petrov-Galerkin finite element scheme for non-ionized hypersonic flows in thermochemical nonequilibrium. *AIAA Paper*, 134:2011, 2011.

[9] Vladimir V Riabov. Approximate calculation of transport coefficients of earth and mars atmospheric dissociating gases. *Journal of thermophysics and heat transfer*, 10(2):209–216, 1996.

[10] Peter A Gnoffo, Roop N Gupta, and Judy L Shinn. Conservation equations and physical models for hypersonic air flows in thermal and chemical nonequilibrium. 1989.

[11] Chul Park. Review of chemical-kinetic problems of future nasa missions. I: Earth entries. *Journal of Thermophysics and Heat transfer*, 7(3):385–398, 1993.

[12] James B Scoggins and Thierry E Magin. Development of mutation++: Multicomponent thermodynamics and transport properties for ionized gases library in C++. *AIAA Paper*, 2966, 2014.

[13] Douglas G Fletcher and Douglas J Bamford. Arcjet flow characterization using laser-induced fluorescence of atomic species. *AIAA paper*, (98-2458):7, 1998.

[14] D Vanden Abeele. *An efficient computational model for inductively coupled air plasma flows under thermal and chemical non-equilibrium*. PhD thesis, PhD Thesis, 2000.

[15] Beno-eth Bottin, David Vanden Abeele, Mario Carbonaro, G. Degrez, and G.S.R Sarma. Thermodynamic and transport properties for inductive plasma modeling. *Journal of thermophysics and heat transfer*, 13(3):343–350, 1999.

[16] Joseph O Hirschfelder, Charles F Curtiss, Robert Byron Bird, and Maria Goeppert Mayer. *Molecular theory of gases and liquids*, volume 26. Wiley New York, 1954.

[17] Walter Guido Vincenti and Charles H Kruger. *Introduction to Physical Gas Dynamics*. John Wiley and Sons Inc., New York, 1965.

[18] Chul Park, Richard L Jaffe, and Harry Partridge. Chemical-kinetic parameters of hyperbolic earth entry. *Journal of Thermophysics and Heat Transfer*, 15(1):76–90, 2001.

[19] Graham V Candler and Robert W MacCormack. Computation of weakly ionized hypersonic flows in thermochemical nonequilibrium. *Journal of Thermophysics and Heat Transfer*, 5(3): 266–273, 1991.

[20] Marco Panesi, Thierry Magin, Anne Bourdon, Arnaud Bultel, and Olivier Chazot. FIRE II flight experiment analysis by means of a collisional-radiative model. *Journal of Thermophysics and Heat Transfer*, 23(2):236–248, 2009.

[21] M Panesi, T Magin, A Bourdon, A Bultel, and O Chazot. Study of electronically excited state populations of atoms and molecules predicted by means of a collisional-radiative model for the FIRE II flight experiment. *Journal of Thermophysics and Heat Transfer*, 25:361–374, 2011.

[22] Marco Panesi, Richard L Jaffe, David W Schwenke, and Thierry E Magin. Rovibrational internal energy transfer and dissociation of n2 (1σg+)- n (4su) system in hypersonic flows. *The Journal of chemical physics*, 138(4):044312, 2013.

[23] Marco Panesi and Andrea Lani. Collisional radiative coarse-grain model for ionization in air. *Physics of Fluids (1994-present)*, 25(5):057101, 2013.

[24] Alessandro Munafò, Marco Panesi, RL Jaffe, Gianpiero Colonna, Anne Bourdon, and TE Magin. Qct-based vibrational collisional models applied to nonequilibrium nozzle flows. *The European Physical Journal D-Atomic, Molecular, Optical and Plasma Physics*, 66(7):1–11, 2012.

[25] A Munafò, M Panesi, and TE Magin. Boltzmann rovibrational collisional coarse-grained model for internal energy excitation and dissociation in hypersonic flows. *Physical Review E*, 89(2): 023001, 2014.

[26] Joel H Ferziger and Hans G Kaper. Mathematical theory of transport processes in gases. 1972.

[27] Jong-Hun Lee. Basic governing equations for the flight regimes of aeroassisted orbital transfer vehicles. 1985.

[28] Jerrold M Yos. Transport properties of nitrogen, hydrogen, oxygen, and air to 30,000 k. Technical report, DTIC Document, 1963.

[29] P.R. Spalart and Steven R. Allmaras. A one-equation turbulence model for aerodynamic flows. 1992.

[30] Ian Christie, David F Griffiths, Andrew R Mitchell, and Olgierd C Zienkiewicz. Finite element methods for second order differential equations with significant first derivatives. *International Journal for Numerical Methods in Engineering*, 10(6):1389–1396, 1976.

[31] Thomas-Peter Fries and Hermann G Matthies. A review of Petrov–Galerkin stabilization approaches and an extension to meshfree methods. *Technische Universitat Braunschweig, Brunswick*, 2004.

[32] Martin P Kessler and Armando M Awruch. Analysis of hypersonic flows using finite elements with Taylor–Galerkin scheme. *International journal for numerical methods in fluids*, 44(12): 1355–1376, 2004.

[33] Bo-Nan Jiang and Graham F Carey. A stable least-squares finite element method for non-linear hyperbolic problems. *International journal for numerical methods in fluids*, 8(8):933–942, 1988.

[34] Bo-Nan Jiang and GF Carey. Least-squares finite element methods for compressible euler equations. *International Journal for Numerical Methods in Fluids*, 10(5):557–568, 1990.

[35] J Taylor Erwin, W Kyle Anderson, Sagar Kapadia, and Li Wang. Three-dimensional stabilized finite elements for compressible Navier–Stokes. *AIAA journal*, 51(6):1404–1419, 2013.

[36] Shahrouz Koohialiabadi. *Parallel finite element computations in aerospace applications*. PhD thesis, University of Minnesota, 1994.

[37] Shahrouz K Aliabadi and Tayfun E Tezduyar. Parallel fluid dynamics computations in aerospace applications. *International Journal for Numerical Methods in Fluids*, 21(10):783–805, 1995.

[38] Gerald John Le Beau. *The finite element computation of compressible flows*. PhD thesis, University of Minnesota, 1990.

[39] Thomas JR Hughes, Leopoldo P Franca, and Gregory M Hulbert. A new finite element formulation for computational fluid dynamics: Viii. the Galerkin/least-squares method for advective-diffusive equations. *Computer Methods in Applied Mechanics and Engineering*, 73 (2):173–189, 1989.

[40] Farzin Shakib, Thomas JR Hughes, and Zdeněk Johan. A new finite element formulation for computational fluid dynamics: X. the compressible Euler and Navier-Stokes equations. *Computer Methods in Applied Mechanics and Engineering*, 89(1):141–219, 1991.

[41] Daryl Lawrence Bonhaus. *A higher order accurate finite element method for viscous compressible flows*. PhD thesis, Virginia Polytechnic Institute and State University, Blacksburg, VA, 1998.

[42] William D Gropp, Dinesh K Kaushik, David E Keyes, and Barry F Smith. High-performance parallel implicit CFD. *Parallel Computing*, 27(4):337–362, 2001.

[43] Paul D Hovland, Lois C McInnes, et al. Parallel simulation of compressible flow using automatic differentiation and PETSc. *Parallel Computing*, 27(4):503–519, 2001.

[44] DK Kaushik, DE Keyes, BF Smith, et al. Newton-krylov-schwarz methods for aerodynamic problems: Compressible and incompressible flows on unstructured grids. In *Proceedings of the 11th International Conference on Domain Decomposition Methods. Domain Decomposition Press, Bergen*, 1999.

[45] George Karypis and Vipin Kumar. Metis-unstructured graph partitioning and sparse matrix ordering system, version 2.0. 1995.

[46] Benjamin Shelton Kirk. *Adaptive finite element simulation of flow and transport applications on parallel computers*. ProQuest, 2007.

[47] S Balay, S Abhyankar, M Adams, J Brown, P Brune, K Buschelman, V Eijkhout, W Gropp, D Kaushik, M Knepley, et al. Petsc users manual revision 3.5. 2014.

[48] Richard Barrett, Michael W Berry, Tony F Chan, James Demmel, June Donato, Jack Dongarra, Victor Eijkhout, Roldan Pozo, Charles Romine, and Henk Van der Vorst. *Templates for the solution of linear systems: building blocks for iterative methods*, volume 43. Siam, 1994.

[49] Gene H Golub and Charles F Van Loan. Matrix computations. johns hopkins series in the mathematical sciences. *Johns Hopkins University Press, Baltimore, MD*, 1989.

[50] Paul T Bauman, Roy Stogner, Graham F Carey, Karl W Schulz, Rochan Updadhyay, and Andre Maurente. Loose-coupling algorithm for simulating hypersonic flows with radiation and ablation. *Journal of Spacecraft and Rockets*, 48(1):72–80, 2011.

[51] John H Lewis Jr and William I Scallion. Flight parameters and vehicle performance for project FIRE flight II, launched may 22, 1965. Technical report, NASA TN D-3569, 1966.

[52] Elden S Cornette. Forebody temperatures and calorimeter heating rates measured during project FIRE 2 reentry at 11.35 kilometers per second. Technical report, NASA TM-X-1305, 1966.

[53] David Hash, Joseph Olejniczak, Michael Wright, Dinesh Prabhu, Maria Pulsonetti, Brian Hollis, Peter Gnoffo, Michael Barnhardt, Ioannis Nompelis, and Graham Candler. FIRE II calculations for hypersonic nonequilibrium aerothermodynamics code verification: Dplr, laura, and us3d. In *45th AIAA Aerospace Sciences Meeting and Exhibit, Reno, NV, Paper No. AIAA-2007-605*, 2007.

[54] Roop N Gupta, Jerrold M Yos, Richard A Thompson, and Kam-Pui Lee. A review of reaction rates and thermodynamic and transport properties for an 11-species air model for chemical and thermal nonequilibrium calculations to 30000 k. Technical report, NASA Langley Research Center, 1990.

[55] Chul Park and Seung-Ho Lee. Validation of multitemperature nozzle flow code. *Journal of thermophysics and heat transfer*, 9(1):9–16, 1995.

[56] Ken-ichi Abe, Tsuyoshi Kameyama, Hisashi Kihara, Michio Nishida, Katsuhiro Ito, and Hideyuki Tanno. Computation and experiment of a nonequilibrium nozzle flow of arc-heated air. *Journal of thermophysics and heat transfer*, 19(4):428–434, 2005.

[57] Kyu Hong Kim, Oh Hyun Rho, and Chul Park. Navier-Stokes computation of flows in arc heaters. *Journal of thermophysics and heat transfer*, 14(2):250–258, 2000.

[58] Takeharu Sakai, Keisuke Sawada, and Masahiko Mitsuda. Application of planck-rosseland-gray model for high-enthalpy arc heaters. *Journal of thermophysics and heat transfer*, 15(2): 176–183, 2001.

[59] Takeharu Sakai and Joseph Olejniczak. Improvements in a Navier-Stokes code for are heater flows. *AIAA Paper*, 3782, 2003.

[60] Jeong-Il Lee, Chongam Kim, and Kyu Hong Kim. Accurate computations of arc-heater flows using two-equation turbulence models. *Journal of thermophysics and heat transfer*, 21(1): 67–76, 2007.

[61] Takeharu Sakai. Computational simulation of high enthalpy arc heater flows. *Journal of thermophysics and heat transfer*, 21(1):77–85, 2007.

[62] Yusuke Takahashi, Takashi Abe, Hiroki Takayanagi, Masahito Mizuno, Hisashi Kihara, and Ken-ichi Abe. Advanced validation of nonequilibrium plasma flow simulation for arc-heated wind tunnels. *Journal of Thermophysics and Heat Transfer*, 28(1):9–17, 2014.